

# North Atlantic tropical cyclone size and storm surge reconstructions from 1950-present

Avantika Gori<sup>1</sup>, Ning Lin<sup>1</sup>, Benjamin Schenkel<sup>2</sup>, and Daniel Chavas<sup>3</sup>

<sup>1</sup>Princeton University

<sup>2</sup>University of Oklahoma/CIMMS/NOAA National Severe Storms Laboratory

<sup>3</sup>Purdue University

November 23, 2022

## Abstract

Tropical cyclones (TCs) are one of the greatest threats to coastal communities along the US Atlantic and Gulf coasts due to their extreme winds, rainfall and storm surge. Analyzing historical TC climatology and modeling TC hazards can provide valuable insight to planners and decision makers. However, detailed TC size information is typically only available from 1988 onward, preventing accurate wind, rainfall, and storm surge modeling for TCs occurring earlier in the historical record. To overcome temporally limited TC size data, we develop a database of size estimates that are based on reanalysis data and a physics-based model. Specifically, we utilize ERA5 reanalysis data to estimate the TC outer size, and a physics-based TC wind model to estimate the radius of maximum wind. We evaluate our TC size estimates using two high-resolution wind datasets as well as Best Track information for a wide variety of TCs. Using the estimated size information plus the TC track and intensity, we reconstruct historical storm tides from 1950-2020 using a basin-scale hydrodynamic model and show that our reconstructions agree well with observed peak water levels. Finally, we demonstrate that incorporating an expanded set of historical modeled storm tides beginning in 1950 can enhance our understanding of US coastal hazard. Our newly developed database of TC sizes and associated storm tides can aid in understanding North Atlantic TC climatology and modeling TC wind, storm surge, and rainfall hazard along the US Atlantic and Gulf coasts.

## Hosted file

supplementary\_information.docx available at <https://authorea.com/users/528576/articles/601716-north-atlantic-tropical-cyclone-size-and-storm-surge-reconstructions-from-1950-present>

1 **North Atlantic tropical cyclone size and storm surge reconstructions**  
2 **from 1950-present**

3

4 Avantika Gori<sup>a</sup>, Ning Lin<sup>a</sup>, Benjamin Schenkel<sup>b,c</sup>, Daniel Chavas<sup>d</sup>

5 <sup>a</sup> *Department of Civil and Environmental Engineering, Princeton University, Princeton, NJ*

6 <sup>b</sup> *The Cooperative Institute for Severe and High-Impact Weather Research and Operations, University of*  
7 *Oklahoma, Norman, OK*

8 <sup>c</sup> *NOAA/OAR National Severe Storms Laboratory, Norman, OK*

9 <sup>d</sup> *Department of Earth, Atmospheric, and Planetary Sciences, Purdue University, West Lafayette, IN*

10

11 *Corresponding Author: Avantika Gori, [agori@princeton.edu](mailto:agori@princeton.edu)*

12

13 **Key Points**

- 14 • We leverage ERA5 reanalysis data combined with a physics-based wind model to  
15 estimate tropical cyclone (TC) storm size
- 16 • We develop a dataset of North Atlantic TC storm sizes (i.e. radius to maximum  
17 wind and outer size) from 1950-2020
- 18 • Using reconstructed TC sizes and a hydrodynamic model, we develop a dataset of  
19 historical storm tides from 1950-2020

20

21 **Abstract**

22 Tropical cyclones (TCs) are one of the greatest threats to coastal communities  
23 along the US Atlantic and Gulf coasts due to their extreme winds, rainfall and storm  
24 surge. Analyzing historical TC climatology and modeling TC hazards can provide  
25 valuable insight to planners and decision makers. However, detailed TC size information  
26 is typically only available from 1988 onward, preventing accurate wind, rainfall, and  
27 storm surge modeling for TCs occurring earlier in the historical record. To overcome  
28 temporally limited TC size data, we develop a database of size estimates that are based on  
29 reanalysis data and a physics-based model. Specifically, we utilize ERA5 reanalysis data  
30 to estimate the TC outer size, and a physics-based TC wind model to estimate the radius  
31 of maximum wind. We evaluate our TC size estimates using two high-resolution wind  
32 datasets as well as Best Track information for a wide variety of TCs. Using the estimated  
33 size information plus the TC track and intensity, we reconstruct historical storm tides  
34 from 1950-2020 using a basin-scale hydrodynamic model and show that our  
35 reconstructions agree well with observed peak water levels. Finally, we demonstrate that  
36 incorporating an expanded set of historical modeled storm tides beginning in 1950 can  
37 enhance our understanding of US coastal hazard. Our newly developed database of TC  
38 sizes and associated storm tides can aid in understanding North Atlantic TC climatology  
39 and modeling TC wind, storm surge, and rainfall hazard along the US Atlantic and Gulf  
40 coasts.

41

42 **1. Introduction**

43 Tropical cyclones (TCs) are one of the largest threats to coastal communities  
44 worldwide (Dullaart et al., 2021), and are the costliest natural hazard impacting the  
45 United States (Smith and Katz, 2013). Landfalling TCs can bring extreme winds, storm  
46 surges, and rainfall to coastal regions, resulting in widespread damages and loss of life.  
47 For example, the Galveston hurricane of 1900 caused at least 6,000 fatalities, and remains  
48 the deadliest US hurricane to date (Cline, 1900). More recently, Hurricanes Katrina  
49 (2005), Sandy (2012), and Harvey (2017) caused extreme flooding due to their rainfall  
50 and storm surges with total damages ranging from \$80-\$150 billion (2022 USD) for each  
51 of the storms (Blake et al., 2013; Blake and Zelinsky, 2017; Knabb et al., 2005). Given

52 the magnitude and frequency of TC-induced catastrophes, it is vital to understand and  
53 characterize the wind, rain and surge hazards from historical hurricanes. Developing  
54 spatially and temporally continuous records of TC storm characteristics and associated  
55 hazards can aid in risk assessment, emergency planning, and mitigation efforts.

56 TC wind, rainfall and surge severity in coastal regions depends on storm  
57 characteristics including intensity (maximum sustained wind speed –  $V_{\max}$  and minimum  
58 central pressure –  $P_{\min}$ ), inner size (i.e. radius to maximum wind –  $R_{\max}$ ), translation  
59 speed, and approach angle to the coast (Irish et al., 2008; Ramos-Valle et al., 2020;  
60 Thomas et al., 2019). Peak storm surges also vary based on geographic characteristics,  
61 such as coastline shape and near-shore bathymetry (Woodruff et al., 2013), while  
62 rainfall rates are sensitive to land topography and land cover characteristics (Zhang et al.,  
63 2018). Aside from features of the synoptic-scale environment (such as vertical wind  
64 shear),  $V_{\max}$  and  $R_{\max}$  are often the two most important storm characteristics controlling  
65 the TC wind field (Chavas et al., 2015), peak rainfall rate (Liu et al., 2019), and peak  
66 storm surge (Bass et al., 2017).

67 Databases of North Atlantic TC tracks and intensities, such as the International  
68 Best Track Archive for Climate Stewardship (IBTrACS; Knapp et al., 2010), date back  
69 to the 1800's. However, detailed TC size estimates are typically only available from 1988  
70 onward (Demuth et al., 2006). There are also numerous databases containing  
71 information about observed TC storm surges and rainfall. For example, several databases  
72 of observed storm tides from tidal gauges (<https://tidesandcurrents.noaa.gov>) and high-  
73 water marks (<https://stn.wim.usgs.gov/FEV>) are available, and these observations can  
74 provide valuable hazard information. However, their spatial coverage is limited based on  
75 the locations of tidal gauges and collected high water marks. For example, along the US  
76 coastline there are only 100 tidal gauges with more than 30 years of data. The relatively  
77 sparse distribution of tidal gauges may not capture peak water levels induced by TCs  
78 (Haigh et al., 2014; Pugh, 1987), and these gauges may fail during high intensity events  
79 (Beven et al., 2008; Fritz et al., 2007). Other storm surge databases drawing from  
80 observations, technical reports, journal articles, and newspapers (Needham et al., 2015;  
81 Needham and Keim, 2012) have estimated the location and magnitude of peak storm  
82 surges for many historical TCs, although they do not provide spatially continuous storm

83 surge estimates for each event. As with storm surge observations, peak wind speed and  
84 rainfall observations are available at gauge locations (Menne et al., 2012) dating back to  
85 the late 1800's. However, spatially continuous, sub-daily wind field or rainfall  
86 observations, such as data derived from satellite and radar, is only available starting in the  
87 late 1990's (Chavas and Vigh, 2014; Huffman et al., 2021; Lin and Mitchell, 2005;  
88 Powell et al., 1998). Moreover, since satellite data is often only available at irregular  
89 sampling intervals, snapshots of wind and rainfall estimates from satellite products may  
90 not be temporally continuous. Given the dearth of observations, we can instead use  
91 physics-based wind models, rainfall models, and high-resolution hydrodynamic models  
92 to reconstruct spatially and temporally continuous estimates of historical TC hazards and  
93 structure. Currently, model-based datasets of historical TC storm tides and winds only  
94 date back to 1988 (Done et al., 2020; Marsooli and Lin, 2018; Muis et al., 2019) due to  
95 temporally limited TC size data. Expanding these datasets to incorporate hazard estimates  
96 from earlier TCs would greatly enhance our understanding of historical TC risk.

97 To overcome temporally limited TC size data, reanalysis datasets, which are  
98 based on operational numerical weather prediction models and data assimilation, and  
99 physics-based TC models may be used together to estimate wind field structure. Typical  
100 global reanalysis products, with horizontal grid resolution ranging from  $0.25^{\circ}$ - $0.7^{\circ}$ , are  
101 often unable to resolve the TC inner core (Hodges et al., 2017; Schenkel and Hart,  
102 2012). However, these datasets may be able to accurately represent features of the outer  
103 TC wind field (Schenkel et al., 2017), where there is minimal convection and the lower  
104 troposphere is approximately in radiative-subsidence balance (Chavas et al., 2015). The  
105 size of the outer TC wind field is often defined as the radius of the outermost closed  
106 isobar (Merrill, 1984), or radius of a specified mean azimuthal weak wind speed (e.g.,  
107 radius of 2 – 12 m/s azimuthal winds; Chavas et al., 2016; Chavas and Vigh, 2014;  
108 Schenkel et al., 2018, 2017). Previous studies have found that reanalysis datasets can  
109 reasonably represent TC outer size metrics, such as radii of azimuthal-mean 6-8 m/s  
110 azimuthal winds (Bian et al., 2021; Schenkel et al., 2017). Using reanalysis-based  
111 estimates of TC outer size and  $V_{\max}$  based on Best Track data, parametric TC wind  
112 models may be used to characterize the full TC wind field. Specifically, the physics-  
113 based complete TC wind model of Chavas et al. (2015; hereafter CLE15) can realistically

114 reproduce the entire TC wind field structure including hard to measure quantities like  
115  $R_{\max}$  based on outer size and  $V_{\max}$  (Chavas et al., 2015; Lin and Chavas, 2012).  
116 Recently, Chavas and Knaff (2022) demonstrated how the CLE15 theory is quite similar  
117 to observations in their effort to create a simple physics-based empirical model to  
118 estimate  $R_{\max}$  from the radius of 17.5 m/s wind that compares well against  $R_{\max}$   
119 observations from historical North Atlantic TCs.

120 In this study, we leverage reanalysis-based estimates of TC outer size and the  
121 physics-based CLE15 wind model to reconstruct North Atlantic historical TC wind fields  
122 from 1950-2020 and model their associated storm tides using a high-resolution  
123 hydrodynamic model. We develop the first spatiotemporally continuous databases of  
124  $R_{\max}$  estimates for North Atlantic TCs from 1950-2020 and associated peak storm tides  
125 for the US Atlantic and Gulf coastline. Our database can supplement size estimates from  
126 IBTrACS or the Extended Best Track Database (EBTRK; Demuth et al. 2006) for storms  
127 occurring earlier than 1988 and can supplement previous storm tide databases (Marsooli  
128 and Lin, 2018; Muis et al., 2019) by similarly providing storm tide reconstructions for  
129 TCs occurring from 1950 onward. To evaluate our outer size and  $R_{\max}$  estimates, we  
130 compare against two high-resolution TC wind field databases (QSCAT-R and HWIND)  
131 as well as against IBTrACS data. We evaluate the accuracy of our size estimates for the  
132 full TC life cycle of storms in both the low (equatorward of 30N) and middle (poleward  
133 of 30N) latitudes, and we investigate the uncertainty in the size estimates for storms  
134 undergoing extratropical transition (ET). Storm tide reconstructions are compared against  
135 observed peak water levels from tidal gauges along the US coastline. Finally, we  
136 demonstrate how our storm tide reconstructions impact storm surge hazard assessment at  
137 various US cities.

138

## 139 **2. Methods**

### 140 *2.1. TC Datasets*

141 North Atlantic TC track, intensity, and pressure information from 1950 onward  
142 are obtained from the IBTrACS Version 4 database (Knapp et al., 2010). To focus on  
143 TCs that can cause non-negligible storm surges, we select storms with maximum wind

144 speed greater than 17 m/s that approach within 200 km of the US coastline, resulting in  
145 467 storms.

146 To estimate the outer TC wind field, we utilize the  $0.25^\circ$  latitude x  $0.25^\circ$   
147 longitude 3-h European Centre for Medium-range Weather Forecasts (ECMWF) ERA5  
148 reanalysis dataset and back-extension (Hersbach et al., 2020). We choose the ERA5  
149 reanalysis due to its relatively fine horizontal grid spacing compared to other reanalysis  
150 datasets, its long temporal coverage (1950-2020), and because previous work (Bian et al.,  
151 2020) demonstrated improved outer size representation of ERA5 compared to previous  
152 reanalyses. We determine the position of each TC within the reanalysis grid by using the  
153 IBTrACS position as a first guess. Then, using the sea-level pressure reanalysis fields we  
154 calculate the centroid of pressure deficit and iteratively adjust the estimated TC center  
155 position based on the method of Nguyen et al. (2014). Once given a center, we calculate  
156 the azimuthal-mean wind field and calculate the radius of a given weak wind speed to  
157 define storm size (details below).

158 Due to the lack of satellite data pre-1980 and data assimilation challenges in the  
159 ERA5 back-extension (ECMWF, 2021), size and storm tide estimates from 1950-1979  
160 have higher uncertainty compared to storms occurring from 1980 onward. Due to the  
161 ERA5 back-extension data assimilation approach, some tropical cyclones from 1950-  
162 1978 are represented with unrealistically intense Pmin values in the reanalysis data. We  
163 do not utilize reanalysis-based Pmin estimates in our study, but the unphysical Pmin  
164 values could impact the reanalysis representation of the outer TC wind field. Despite  
165 larger uncertainties associated with size estimates for 1950-1979 TCs, a comparison of  
166 the ERA5 size distributions pre- and post-1980 demonstrates that both groups of storms  
167 have similar outer size climatologies (Figure S1) and similar  $R_{\max}$  climatology (Figure  
168 S2), suggesting that limitations within the 1950-1979 ERA5 data do not cause large  
169 changes in the estimated TC sizes. As subsequent ERA5 1950-1978 versions are released,  
170 our estimated size and storm surge estimates will be updated.

171 To validate reanalysis TC size estimates, we compare against IBTrACS and two  
172 detailed TC wind field databases: the QuikSCAT Tropical Cyclone Radial Structure  
173 database (QSCAT-R; Chavas and Vigh, 2014) and the HWind database (Powell et al.,  
174 1998). Both QSCAT-R and HWind have been widely used to investigate features of the

175 inner (Chavas and Lin, 2016) and outer (Bian et al., 2021; Chavas et al., 2016; Schenkel  
176 et al., 2017) wind fields of historical TCs. QSCAT-R contains snapshots of azimuthal-  
177 mean 10-m azimuthal winds from 167 North Atlantic TCs between 2000-2009, and has a  
178 horizontal grid spacing of approximately 12.5 km. The HWind data used here comes  
179 from 120 North Atlantic TCs spanning 2004-2013 with approximate horizontal grid  
180 spacing of 6 km. QSCAT-R wind fields, which are based on NASA’s QuikSCAT satellite  
181 (Chavas and Vigh, 2014), are available at irregular time points during each TC, while the  
182 HWind data is provided at 6-h intervals. QuikSCAT tends to underestimate wind speeds  
183 in high wind regimes (Stiles et al., 2014) and is therefore more suitable for investigating  
184 features of the outer TC wind field. We utilize the QSCAT-R dataset to validate the outer  
185 TC size estimates and use the higher resolution HWind dataset and IBTrACS data from  
186 2004-2020 to validate the  $R_{\max}$  estimates. Importantly,  $R_{\max}$  estimates from IBTrACS are  
187 not reanalyzed post-storm and are based on near real-time information from aircraft  
188 reconnaissance or remotely-sensed data. Therefore, the IBTrACS  $R_{\max}$  values may have  
189 significant uncertainty or errors. We utilize estimates of the IBTrACS  $R_{\max}$  uncertainty  
190 that were developed by the National Hurricane Center (NHC) based on the 2021 North  
191 Atlantic and Northeast Pacific TC season (C. Landsea, personal communication, March  
192 2022). The uncertainty estimates are based on mean absolute errors (MAEs) for the Best  
193 Track  $R_{\max}$  values and are binned according to TC intensity (Table S1). The MAEs used  
194 here assume each storm is observed by both satellite and aircraft reconnaissance.  
195 Therefore, they represent conservative estimates of uncertainty as points far from land or  
196 without aircraft/satellite observations likely have much higher uncertainty. Moreover, as  
197 these estimates are derived from 2021 data, older storms in the IBTrACS dataset likely  
198 also have higher uncertainty. Nevertheless, the Best Track  $R_{\max}$  errors described here  
199 provide a benchmark we can use to evaluate our model based  $R_{\max}$  estimates.

200

## 201 *2.2. TC Outer Size Estimation*

202 Following Schenkel et al. (2017), we incorporate six outer size metrics defined as  
203 the radii at which the 10-m azimuthal-mean azimuthal wind speed equals 2, 4, 6, 8, 10,  
204 and 12 m/s (denoted  $r_2 - r_{12}$ ). We consider a range of size metrics since not all wind radii  
205 may be defined at every point in time in the reanalysis data. To estimate each size metric

206 at each point in time, we follow Chavas and Vigh (2014). A TC-relative polar coordinate  
207 is constructed and the reanalysis zonal and meridional winds are interpolated into the  
208 polar grid, excluding all grid points over land. A uniform environmental wind is then  
209 removed from the TC-relative zonal and meridional winds, which is estimated as 55% of  
210 the translation speed and rotated 20 degrees counterclockwise according to Lin and  
211 Chavas (2012). An asymmetry parameter ( $\chi$ ) is also calculated at each radius according  
212 to Chavas and Vigh (2014). The  $\chi$  parameter varies from 0 (perfect data symmetry about  
213 the TC center) to 1 (complete asymmetry about the TC center) and quantifies the degree  
214 of data coverage asymmetry at each radial distance. Radial bins with  $\chi > 0.5$  are excluded  
215 from the outer size estimation (Chavas and Vigh, 2014). The azimuthal-mean azimuthal  
216 wind is then calculated, and followed by the extraction of outer size metrics (i.e.  $r_2$ ,  $r_4$ ,  $r_6$ ,  
217  $r_8$ ,  $r_{10}$ ,  $r_{12}$ ).

218 The reanalysis outer size estimates may be biased compared to the observations,  
219 especially for the  $r_{10}$  and  $r_{12}$  metrics (Schenkel et al., 2017). Therefore, we bias correct  
220 each outer size metric based on the comparison with the QSCAT-R outer sizes for the  
221 period between 2000-2009. We find that the average outer size bias is generally constant  
222 across the range of outer sizes for most size metrics (Figure S2), implying that the outer  
223 size estimates can be corrected by simply adding a single correction value to each  
224 estimate for a given metric. For each size metric (i.e.  $r_2$ – $r_{12}$ ), the median difference  
225 between the QSCAT-R values and the ERA5 estimates (shown as the horizontal red lines  
226 in Figure 2a) are calculated and added to each ERA5 size estimate, similar to Bian et al.  
227 (2021). Bias correction is applied to outer size estimates for all TCs from 1950 onward.

228

### 229 *2.3. Physics-based TC wind model and $R_{max}$ estimation*

230 Several parametric TC wind models have been developed to represent the radial  
231 profile of wind speed, and most models require free-fitting parameters as well as  
232 estimates of  $V_{max}$  and  $R_{max}$  (Emanuel and Rotunno, 2011; Holland, 1980; Willoughby  
233 et al., 2006). In contrast, the more recently developed CLE15 complete wind profile is a  
234 fully physics-based model that describes the full TC wind field by merging solutions for  
235 the inner convective region and the outer descending region. Wang et al. (2022) found  
236 that the CLE15 model better reproduces observed TC wind fields compared to the

237 popularly used Holland model (Holland, 1980). As explained in Chavas and Lin (2016),  
238 the CLE15 wind profile can be constructed using  $V_{max}$  and a single additional outer wind  
239 radius. Chavas and Lin (2016) also demonstrated that CLE15 profiles based on  $V_{max}$  and  
240 outer size were able to reproduce the observed wind field variability of historical North  
241 Atlantic TCs. Therefore, we use the CLE15 model to construct the full wind profile and  
242 extract an estimate for  $R_{max}$  using the reanalysis-based outer size estimates and  $V_{max}$  from  
243 IBTrACS. More details about the CLE15 model formulation are documented in Chavas  
244 et al. (2015).

245

#### 246 *2.4 Time series of TC size estimates*

247 A time series of  $R_{max}$  estimates are developed for each TC from 1950-2020 to  
248 match the IBTrACS time steps. For each 3-h increment, the TC outer size metrics ( $r_2-r_{12}$ )  
249 are estimated from the ERA5 reanalysis data, and bias corrected as explained above.  
250 Next, the maximum azimuthal-mean azimuthal wind ( $V_{max}^*$ ) is calculated based on the  
251 IBTrACS  $V_{max}$  ( $V_{max,BT}$ ) as follows:

$$252 \quad V_{max}^* = 0.75(V_{max,BT} - 0.55V_{trans}) \quad (1)$$

253 where  $V_{trans}$  is the TC translation speed. We remove the background wind, estimated as  
254 55% of the storm translation speed (Lin and Chavas, 2012), from  $V_{max,BT}$  and then apply  
255 an additional 0.75 reduction factor similar to the reduction factor of 0.8 used in Chavas et  
256 al. (2016). This additional reduction factor takes into account that  $V_{max,BT}$  represents the  
257 maximum wind speed occurring at any point in the TC, while we are interested in the  
258 maximum azimuthal-mean wind speed. The 0.75 reduction factor was developed by  
259 comparing the IBTrACS  $V_{max}$  estimates for all TCs from 2004-2013 with at least tropical  
260 storm intensity ( $>17$  m/s) against the HWind maximum azimuthal-mean wind speeds  
261 (Figure S3).

262 Using each outer size estimate and  $V_{max}^*$ , we construct a radial profile of  
263 azimuthal-mean 10-m TC azimuthal winds using the CLE15 wind model and estimate  
264  $R_{max}$ . If more than three outer size metrics are undefined for a particular time step,  $R_{max}$  is  
265 set as undefined. Since the CLE15 model may produce different  $R_{max}$  estimates using  
266 different outer size metrics, we create a weighted average  $R_{max}$  based on all defined outer  
267 size metrics with weights equal to the inverse of the root mean square error between the

268 reanalysis outer size estimates and the QSCAT-R outer size estimates (Table S2). Once  
269 the TC makes landfall, we do not utilize the reanalysis data to estimate outer size since  
270 our methodology sets reanalysis 10-m wind speeds over land are as undefined. Instead,  
271 we assume constant outer size after landfall equal to the last outer size estimate before  
272 landfall. Although TC size can change significantly after landfall (Chen and Chavas,  
273 2020; Hlywiak and Nolan, 2021), our primary goal is to reconstruct TC storm surges,  
274 which would be minimally impacted by size changes occurring after landfall. The  $R_{\max}$  at  
275 each point after landfall is estimated using  $V_{\max}^*$  and constant outer size. Finally, we  
276 apply linear interpolation to fill in time steps where  $R_{\max}$  is undefined due to insufficient  
277 outer size data, leading to a continuous time history of  $R_{\max}$  values for each TC.

278

### 279 *2.5 Defining Extratropical Transition (ET) Storms*

280 Our study objectively defines extratropical transition (ET) using the cyclone  
281 phase space (Hart 2003; Evans and Hart 2003). ET start is defined when the TC  
282 transitions from a warm-core, nonfrontal cyclone to a warm-core, frontal cyclone. This  
283 occurs in the cyclone phase space when the storm-motion-relative 900–600-hPa layer  
284 thickness asymmetry across the TC exceeds an empirical value of 10 m. Positive  
285 thickness asymmetry parameter values correspond to cold and/or dry air to the left of  
286 motion and warm and/or moist air to the right of motion (Hart 2003; Evans and Hart  
287 2003). ET end occurs when the TC transitions from a warm-core, frontal cyclone to a  
288 cold-core, frontal cyclone. This is defined as when the 900–600-hPa thermal wind  
289 changes from positive to negative. Negative values are associated with increases in the  
290 strength of the cyclone wind field with height (Hart 2003). Both cyclone phase space  
291 parameters are calculated over a 500-km radius from the TC center, which is the  
292 approximate length scale of North Atlantic TC outer size (Chavas et al. 2016; Schenkel et  
293 al 2018). We use ERA5 data available at intervals between 25-50 hPa to compute these  
294 parameters.

295

### 296 *2.6 Estimating missing $P_{\min}$ data*

297 For TCs occurring before 1975,  $P_{\min}$  data is missing for some IBTrACS time  
298 steps. Although  $P_{\min}$  is not a required input when estimating the storm  $R_{\max}$ ,  $P_{\min}$  does

299 impact the modeled storm surge since the low-pressure TC center causes a small rise in  
300 ocean water level. The missing  $P_{min}$  data can be estimated using a simplification of the  
301 cyclostrophic balance equation (Knaff and Zehr, 2007):

$$302 \quad P_{min} = P_{ref} - \left(\frac{v_{max}}{c}\right)^{1/n} \quad (2)$$

303 where  $C$  and  $n$  are empirically-derived coefficients that vary with latitude and were  
304 computed in Landsea et al. (2004), Table 7.5. Alternately, gradient wind balance can be  
305 used to relate the radial profiles of pressure and azimuthal wind speed, with the wind  
306 speed profile specified by the CLE15 model. Previous work by Chavas et al. (2017)  
307 showed that the application of the gradient wind balance theory can accurately predict the  
308 storm pressure deficit. A comparison of  $P_{min}$  estimated using the empirical cyclostrophic  
309 balance equation (2) and the gradient wind balance with CLE15 wind profile yielded  
310 similar results (Figure S4). Since calculating  $P_{min}$  using the gradient wind balance is more  
311 computationally expensive, we opt to use the simplified cyclostrophic balance equation in  
312 place of missing data.

313

## 314 *2.7 Hydrodynamic modeling of TCs*

315 To reconstruct storm tides from historical TCs, we couple the CLE15 wind model  
316 with the 2D, depth-integrated version of the advanced circulation (ADCIRC)  
317 hydrodynamic model (Luettich et al., 1992; Westerink et al., 1992). We utilize an  
318 unstructured computational mesh that spans the entire North Atlantic basin and has  
319 relatively high coastal resolution ( $\sim 1$  km). The mesh was developed and validated in  
320 Marsooli and Lin (2018). We also incorporate forcing from eight tidal constituents,  
321 which are estimated from the global model of ocean tides TPXO8-ATLAS (Egbert and  
322 Erofeeva, 2002). Recently, Wang et al. (2022) showed more accurate estimates of peak  
323 storm tides in ADCIRC when it was coupled to the CLE15 model compared to the  
324 Holland wind model. Based on the track, intensity and size time histories of each TC,  
325 ADCIRC simulates peak storm tides along the US Atlantic and Gulf coasts.

326 We compare our storm tide reconstructions to observed peak water levels from 74  
327 NOAA tidal gauges (<https://tidesandcurrents.noaa.gov>) located along the US Atlantic and  
328 Gulf coasts. Observed water levels from all active tidal gauges within 200 km of each TC

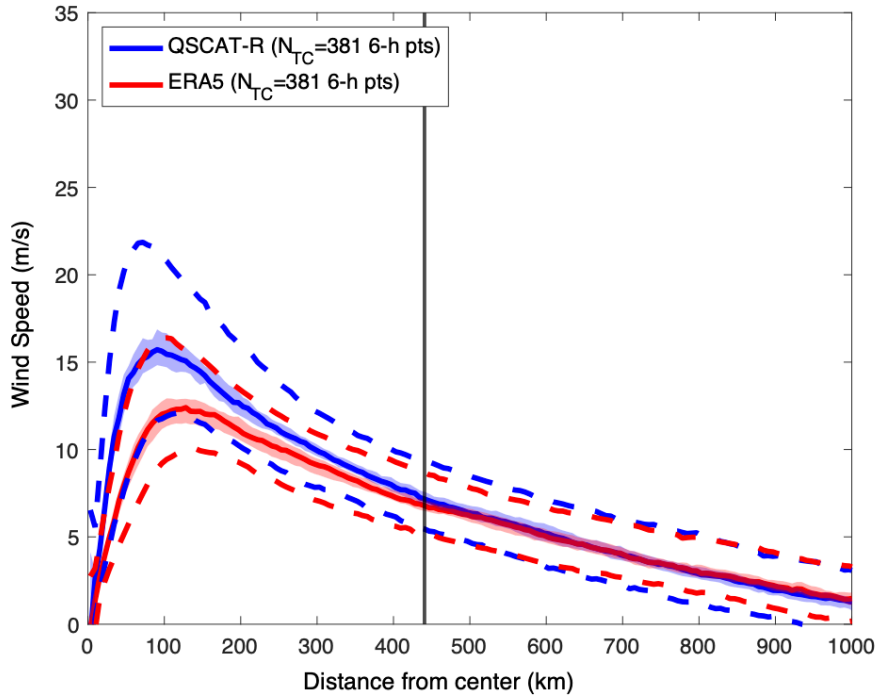
329 track are compared against simulated storm tides. Gauges that were malfunctioning,  
330 located within river or estuaries, or where water levels were clearly impacted by  
331 freshwater discharges are excluded from the comparison. We divide the coastline into  
332 five regions: western Gulf of Mexico (extending until New Orleans, LA), eastern Gulf of  
333 Mexico, southeast Atlantic (until Chesapeake Bay), mid-Atlantic (until Connecticut), and  
334 New England. Tidal gauges are grouped within each region to evaluate how well the  
335 storm surge reconstructions match observations for different portions of the coast.

336

### 337 **3. Results**

#### 338 *3.1 Representation of TC wind field within ERA5 reanalysis*

339 We first compare the radial structure of TC mean azimuthal wind from the ERA5  
340 reanalysis and the QSCAT-R data. Figure 1 shows the median azimuthal-mean azimuthal  
341 wind profile across all 6-h TC time steps between 2000-2009 with at least tropical storm  
342 intensity from ERA5 and QSCAT-R. Although previous work found that ERA5 better  
343 resolves TCs compared to the earlier ERA-Interim (Bian et al., 2021; Dullaart et al.,  
344 2020), Fig. 1 shows that the reanalysis data still largely under resolves inner TC wind  
345 speeds as expected from prior work (Schenkel et al. 2012; Schenkel et al. 2017). The  
346 ERA5 data also overestimates  $R_{\max}$  (Fig. 1) likely in part because of its coarse horizontal  
347 resolution and conservative physics parameterizations (Schenkel et al. 2017; Bian et al.  
348 2021). However, Fig. 1 also shows that ERA5 represents the outer TC wind field  
349 accurately compared to QSCAT-R (Bian et al. 2021). For  $r > 440$  km, the median wind  
350 profiles from the two datasets converge, and a Kolmogorov-Smirnov test at the 5% level  
351 suggests that wind speeds from both datasets at each subsequent radii come from the  
352 same distribution. The comparison of the wind profiles illustrates that ERA5 is a  
353 reasonable source for estimating features of the outer wind field.



354

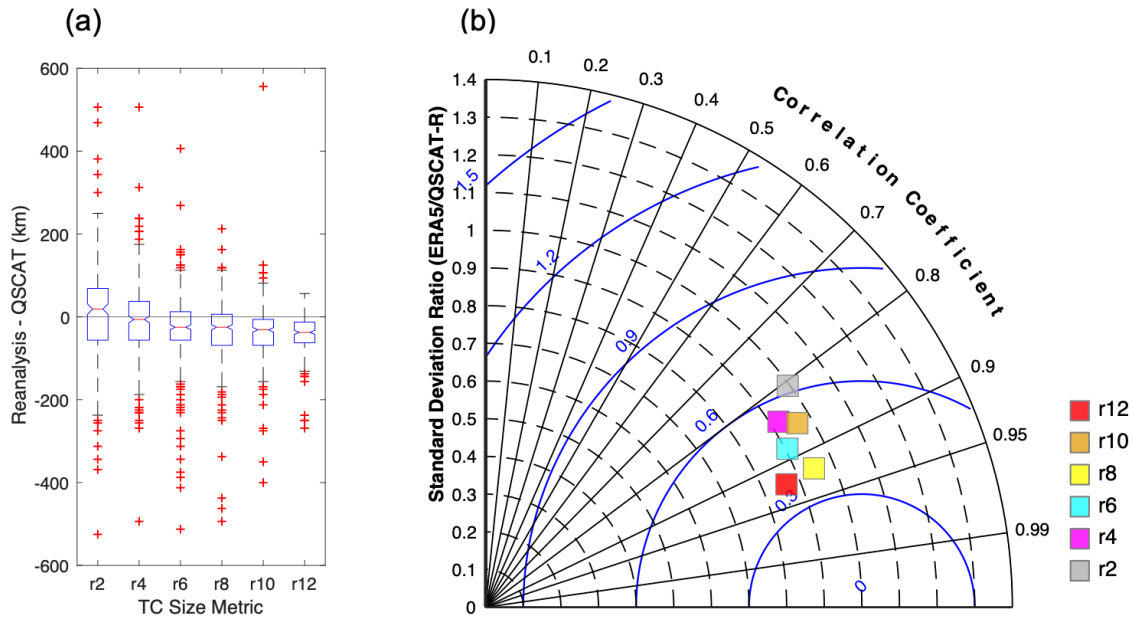
355 **Figure 1:** Median azimuthal wind profile (solid) with boot-strapped 95% confidence bounds  
 356 (shaded) and inter-quartile range (IQR - dashed) for all QSCAT TC snapshots with  $V_{max}$   
 357 greater than 17 m/s.  
 358

### 359 3.2 Accuracy of reanalysis-derived outer size metrics

360 After establishing that the TC outer wind profile from the ERA5 compares well to  
 361 QSCAT-R, we next evaluate the accuracy of ERA5 outer size estimates. For each  
 362 QSCAT-R data point and outer size metric (i.e.  $r_2$ ,  $r_4$ ,  $r_6$ ,  $r_8$ ,  $r_{10}$ , and  $r_{12}$ ), we compare  
 363 against the corresponding ERA5 sizes. The outer size analysis includes 381 QSCAT-R  
 364 snapshots, although the size metrics are not all defined for each snapshot. Figure 2a  
 365 shows boxplots of the difference between ERA5 and QSCAT-R for each size metric.  
 366 Except for  $r_2$ , ERA5 slightly underestimates the outer size compared to QSCAT-R, with a  
 367 larger negative bias for  $r_{10}$  and  $r_{12}$ . In contrast, the variability of the size estimates  
 368 decreases for radii of higher wind speeds, demonstrated by the narrower interquartile  
 369 ranges for  $r_{10}$  and  $r_{12}$ . The larger negative bias for  $r_{10}$  and  $r_{12}$  is due to ERA5 consistently  
 370 under-predicting wind speeds for radial distances closer than 440 km (Fig. 1a) as found in  
 371 previous studies (Bian et al., 2021; Schenkel et al., 2017).

372 Figure 2b shows a Taylor diagram (Taylor, 2001) comparing outer size in the  
 373 ERA5 versus QSCAT-R. There is high correlation between ERA5 and QSCAT-R for all

374 size metrics, ranging from 0.8-0.93, with the highest correlations for  $r_{12}$  and  $r_8$ . The ratio  
 375 of the standard deviations ranges from 0.8-1, indicating that there is less variability in the  
 376 ERA5 sizes compared to QSCAT-R. The  $r_{12}$  and  $r_8$  metrics have the lowest root-mean-  
 377 square-error (RMSE), followed by  $r_6$ ,  $r_{10}$ ,  $r_4$ , and lastly  $r_2$ . As found in Schenkel et al.  
 378 (2017), the lower correlation coefficient, higher RMSE, and higher normalized standard  
 379 deviation for the  $r_2$  metric suggests that the reanalysis data struggles to resolve weak  
 380 azimuthal-mean TC wind speeds from the environmental background wind. Nevertheless,  
 381 based on the relatively high correlation coefficients, low RMSE, and good match to  
 382 QSCAT-R based outer sizes (Figure S3) for most other size metrics, the ERA5 reanalysis  
 383 outer size estimates can be used (after bias correction) to realistically represent the outer  
 384 TC wind field.

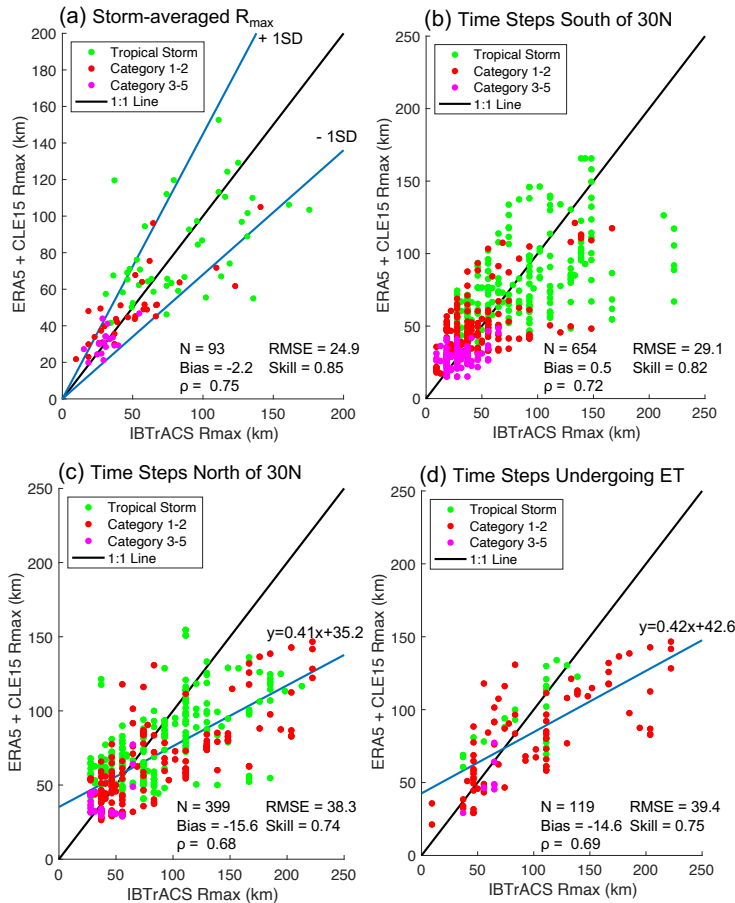


385  
 386 **Figure 2:** (a) Boxplots of outer size error of ERA5 reanalysis data compared to QSCAT-R for 381  
 387 TC snapshots at radii at which the azimuthal-mean 10-m azimuthal wind equals 12 m/s  
 388 ( $r_{12}$ ), 10 m/s ( $r_{10}$ ), 8 m/s ( $r_8$ ), 6 m/s ( $r_6$ ), 4 m/s ( $r_4$ ) and 2 m/s ( $r_2$ ). Median of each  
 389 metric shown as horizontal red line, and width of notch on each box denotes 95%  
 390 uncertainty bounds of the median, calculated through bootstrapping. Red plus signs  
 391 denote outliers using  $1.5 \cdot \text{IQR}$  formula. (b) Pearson correlation (radial axis), ratio of  
 392 standard deviations (y axis), and root mean square error (RMSE) between ERA5 and  
 393 QSCAT (blue contours) for each outer size metric.

### 395 3.3 Accuracy of $R_{max}$ estimates

396 The ERA5 outer size estimates at each TC time step are bias corrected by adding  
 397 the median difference between ERA5 and QSCAT-R outer size (red lines in Figure 2a)

398 calculated for each size metric (see Section 2.2). Then, using the bias corrected outer size  
 399 estimates and  $V_{\max}^*$  defined in equation 1, we compute the azimuthal-mean 10-m wind  
 400 field for each TC time step based on the CLE15 model and extract  $R_{\max}$ . We compare the  
 401 ERA5+CLE15  $R_{\max}$  values against  $R_{\max}$  values from IBTrACS (Figure 3) and the high-  
 402 resolution HWind dataset (Figure S5). Figure 3a shows a comparison of storm-averaged  
 403  $R_{\max}$  for each TC between 2004-2020 for the duration of time when the TC is at least 100  
 404 km away from land and has intensity  $> 17.5$  m/s. Figures 3b-e show a comparison of all  
 405 6-h time steps between 2004-2020 with intensity  $> 17.5$  m/s and a distance to land of at  
 406 least 100 km. Similarly, Figure S5 shows the same comparison for TC snapshots taken  
 407 from HWind. The HWind  $R_{\max}$  comparison illustrates that the model performs well  
 408 overall: the RMSE is 31 km and the mean bias is only 0.3 km. Apart from a couple  
 409 tropical storm intensity outliers, the vast majority of TC snapshots in Fig. S5 are clustered  
 410 around the 1:1 line.



411

412

413

**Figure 3:** (a) Comparison between storm-averaged  $R_{\max}$  using ERA5 outer size and CLE15 wind profile (ERA5+CLE15) and IBTrACS  $R_{\max}$  for TCs where  $V_{\max}$  is greater than 17 m/s. Points

414 are colored by their Saffir-Simpson category. (b) Same as in (a) except using each 6-hour TC  
415 time step for TCs below 30 degrees latitude, (c) same as in b but for TC time steps above 30  
416 degrees latitude, (d) same as in b but for extra-tropical transitioning (ET) time steps, where ET is  
417 defined according to the cyclone phase space (Hart, 2003).  
418

### 419 3.3.1 Storm-Averaged Performance

420 Figure 3a shows a comparison between storm averaged  $R_{\max}$  using ERA5+CLE15  
421 and IBTrACS.  $R_{\max}$  performance is quantified using three metrics: the RMSE, mean bias,  
422 and Willmott skill (Willmott, 1981), which quantifies the degree of agreement between  
423 modeled and observed data and ranges from 0 (complete disagreement) to 1 (complete  
424 agreement). The overall storm-averaged performance is relatively good, with a Willmott  
425 skill of 0.85 and average bias of -2.2 km. The variability in the difference between  
426 ERA5+CLE15 and IBTrACS increases with increasing  $R_{\max}$ , suggesting that there is  
427 higher uncertainty for large  $R_{\max}$  values. Additionally, the ERA5+CLE15 approach  
428 performs better in terms of storm averaged  $R_{\max}$  for hurricane strength (>33 m/s) storms  
429 (red and magenta points) compared to tropical storm intensity (<33 m/s) events (green  
430 points), which tend to have larger  $R_{\max}$  values. The lower ERA5+CLE15 performance for  
431 tropical storm intensity TCs could also be due to challenges extracting reanalysis outer  
432 size estimates from weak, less organized storms.

433 To measure the uncertainty associated with the ERA5+CLE15  $R_{\max}$  estimates, we  
434 develop a low and high estimate in addition to the modeled  $R_{\max}$ . We first calculate the  
435 percent difference between the IBTrACS and ERA5+CLE15 storm averaged  $R_{\max}$  values,  
436 which has a mean of approximately 0%. Then we scale all the  $R_{\max}$  values up (down) by  
437 one standard deviation of the percent difference to get the high (low) estimate. Using this  
438 procedure, the low-high estimates overlap with the IBTrACS values for 68% of storms  
439 (close to +/- one standard deviation range of a normal distribution) shown in Fig. 3a.

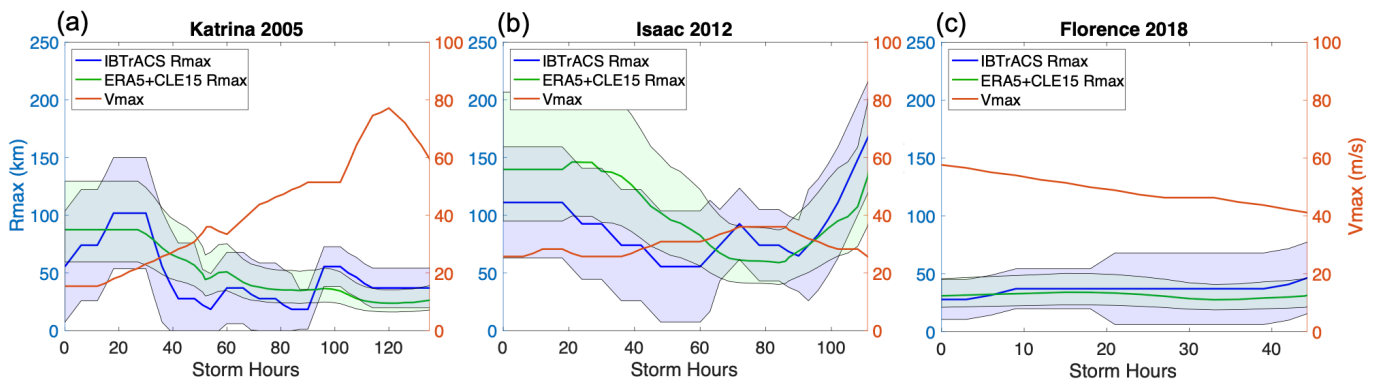
440

### 441 3.3.2 Performance for Low-Latitude TCs

442 Fig. 3b shows the comparison between ERA5+CLE15 and IBTrACS  $R_{\max}$  at each  
443 time step where a TC is below 30° N latitude. The ERA5+CLE15 approach performs  
444 well for low latitude TCs, with a mean bias of only 0.5 km and RMSE of 29.1 km. There  
445 are a few very large, weak TCs occurring below 30° N that are underestimated by  
446 ERA5+CLE15, and a few category 1-2 TC time steps that are also underestimated.

447 However, most TC time steps occurring below 30° N correlate well with the IBTrACS  
 448  $R_{max}$  and fall within the IBTrACS uncertainty bounds.

449 To further illustrate the performance of the modeled  $R_{max}$  values at low latitudes,  
 450 Figure 4 shows the temporal evolution of  $R_{max}$  until landfall (where the plots terminate)  
 451 based on ERA5+CLE15 (green) and IBTrACS  $R_{max}$  (blue) for three hurricanes that  
 452 encompass a wide range of  $R_{max}$  evolution: (a) Katrina (2005), (b) Isaac (2012), and (c)  
 453 Florence (2018). The model-based (+/- standard deviation) and IBTrACS (+/- MAE)  $R_{max}$   
 454 uncertainty ranges are also shown on each plot as shaded regions. For Isaac and Florence,  
 455 the temporal evolution of modeled  $R_{max}$  tracks well with IBTrACS, as the ERA5+CLE15  
 456 approach is able to capture the shrinking/expanding TC size evolution. For Katrina's  
 457 case, there is an increase in  $R_{max}$  occurring around hour 90 that is underestimated by  
 458 ERA5+CLE15. Across all three storms the ERA5+CLE15  $R_{max}$  values fall within the  
 459 IBTrACS uncertainty bounds for the vast majority of time steps. Additionally, in most  
 460 cases the IBTrACS values also fall within the ERA5+CLE15 uncertainty range. In the  
 461 case of Isaac, the model initially overestimates  $R_{max}$ , but the ERA5+CLE15 and  
 462 IBTrACS values converge as the storm intensifies. The examples shown in Figure 4  
 463 demonstrate that the ERA5+CLE15  $R_{max}$  values can realistically reproduce TC size  
 464 evolution for landfalling storms.



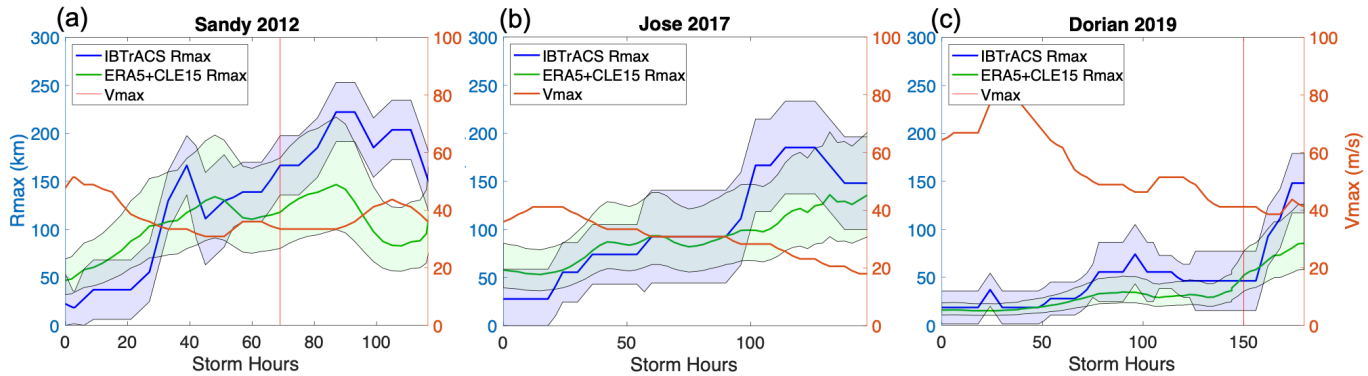
465 **Figure 4:** Evolution of IBTrACS  $R_{max}$  (blue) and ERA5+CLE15  $R_{max}$  (green) with uncertainty  
 466 bounds (shaded area), and  $V_{max}$  (orange) for several major historical TCs occurring below  
 467 30N: (a) Katrina 2005, (b) Isaac 2012, (c) Florence 2018. ERA5+CLE15 uncertainty bounds  
 468 are based on +/- one standard deviation (section 3c.1) and IBTrACS uncertainty bounds  
 469 are based on +/- mean absolute error (MAE) as estimated by NHC.  
 470  
 471

### 472 3.3.3 Performance at Mid-Latitudes and for ET Storms

473 In contrast to the good performance at low latitudes, the performance of  
474 ERA5+CLE15 is not as good for mid-high latitude storms (Fig. 3c) where the model  
475 tends to underestimate  $R_{max}$  for large storms, resulting in a mean bias of -15.6 km. The  
476 performance of ERA5 + CLE15 is also not as good for extratropical transitioning (ET)  
477 time steps (Fig. 3d), where ET time points are selected based on the cyclone phase space  
478 discussed in section 2.5. As shown in Figs. 3c and 3d, the majority of mid-latitude  
479 hurricane time steps (red points) whose sizes are underestimated by ERA5+CLE15 were  
480 also undergoing ET. Storm ET often results in an expansion and asymmetric evolution of  
481 the wind field (Evans and Hart, 2008; Hart and Evans, 2001; Jones et al., 2003),  
482 causing an increase in  $R_{max}$  (Evans et al., 2017; Evans and Hart, 2008; Halverson and  
483 Rabenhorst, 2013) that is demonstrated by the large  $R_{max}$  for category 1-2 storms shown  
484 in Fig. 3e. ET dynamics are not explicitly captured by the ERA5+CLE15 approach since  
485 the CLE15 wind profile is based on the angular momentum distribution of a mature TC.  
486 Still, ET wind field expansion could be partially accounted for in the ERA5+CLE15  $R_{max}$   
487 estimates: the ERA5-based outer size estimates may capture the expansion in the outer  
488 wind field during ET, and a larger outer size would yield a larger  $R_{max}$  using the CLE15  
489 profile (for fixed intensity and latitude). Similarly, decreasing storm intensity and  
490 increasing latitude (both of which are also associated with ET) would yield increased  
491  $R_{max}$  estimates from the CLE15 model.

492 Figure 5 shows the ERA5+CLE15  $R_{max}$  (green) and IBTrACS  $R_{max}$  (blue)  
493 evolution for three TCs reaching the mid latitudes where ERA5+CLE15 does not perform  
494 as well: (a) Sandy (2012), (b) Jose (2017) and (c) Dorian (2019), where the vertical red  
495 line on each plot indicates ET start and the plot terminates either when the TC makes  
496 landfall or completes ET. In Sandy's case, the  $R_{max}$  had already begun expanding rapidly  
497 before ET started (according to the phase space criteria) as it transitioned from a TC into  
498 a warm-seclusion extratropical cyclone that had both tropical (warm core) and extra-  
499 tropical (frontal structure) features (Halverson and Rabenhorst, 2013). ERA5+CLE15  
500 generally captures Sandy's  $R_{max}$  evolution until ET begins, at which point the IBTrACS  
501  $R_{max}$  increases at a much faster rate than the model predicts, demonstrating that  
502 ERA5+CLE15 can capture some size expansion during ET but not completely. Similarly,  
503 during Dorian the modeled  $R_{max}$  expands once ET begins (Fig. 5c). However, the

504 IBTrACS  $R_{\max}$  expanded at a faster rate during ET than was predicted by the model.  
 505 Hurricane Jose (Fig. 5b) did not undergo ET according to the phase space criteria, but as  
 506 the storm moved north it acquired some extra-tropical characteristics, which caused an  
 507 increase in the storm's  $R_{\max}$  (Berg, 2018).



508 **Figure 5:** Evolution of IBTrACS  $R_{\max}$  (blue) and ERA5+CLE15  $R_{\max}$  (green) with uncertainty  
 509 bounds (shaded area), and  $V_{\max}$  (orange) for several major historical TCs reaching above  
 510 30 N: (a) Sandy (2012), (b) Jose (2017), and (c) Dorian (2019). ERA5+CLE15 uncertainty  
 511 bounds are based on +/- one standard deviation (section 3c.1) and IBTrACS uncertainty  
 512 bounds are based on +/- mean absolute error (MAE) as estimated by NHC. Vertical red line  
 513 indicates time when extra-tropical transition (ET) begins according to the cyclone phase  
 514 space and plots terminate when TC makes landfall or completes ET.  
 515  
 516

517 The ERA5+CLE15  $R_{\max}$  estimates for mid-latitude and ET storms cannot be  
 518 corrected using a simple linear fit against the IBTrACS data. Figs 3c and 3e show that  
 519 ERA5+CLE15 performs well for TC time steps where  $R_{\max}$  is less than roughly 120 km  
 520 (see small storms clustered around the 1:1 line) but tends to largely underestimate  $R_{\max}$   
 521 for larger storms (see divergence from 1:1 line for large storms). For example, the mean  
 522 bias for mid-latitude (ET) storms with  $R_{\max}$  smaller than 120 km is only -2 km (-2.6 km),  
 523 but is -60 km (-60 km) for mid-latitude (ET) storms larger than 120 km. However, the  
 524 uncertainty associated with the IBTrACS  $R_{\max}$  values may be larger for ET storms since  
 525 the  $R_{\max}$  is generally calculated as the location of highest wind speed occurring anywhere  
 526 in the storm (compared to location of highest azimuthal-mean wind speed) and ET storms  
 527 may have non-negligible asymmetry. Despite the larger negative bias and higher  
 528 uncertainty for large ET storms, the ERA5+CLE15 approach produces reasonable TC  
 529 size estimates that can be utilized for hazard analysis. Storm tides along the Mid-Atlantic  
 530 and New England coastlines are less sensitive to  $R_{\max}$  compared to other coastal regions  
 531 (see section 3.4) and errors in  $R_{\max}$  during ET do not result in large errors in peak storm

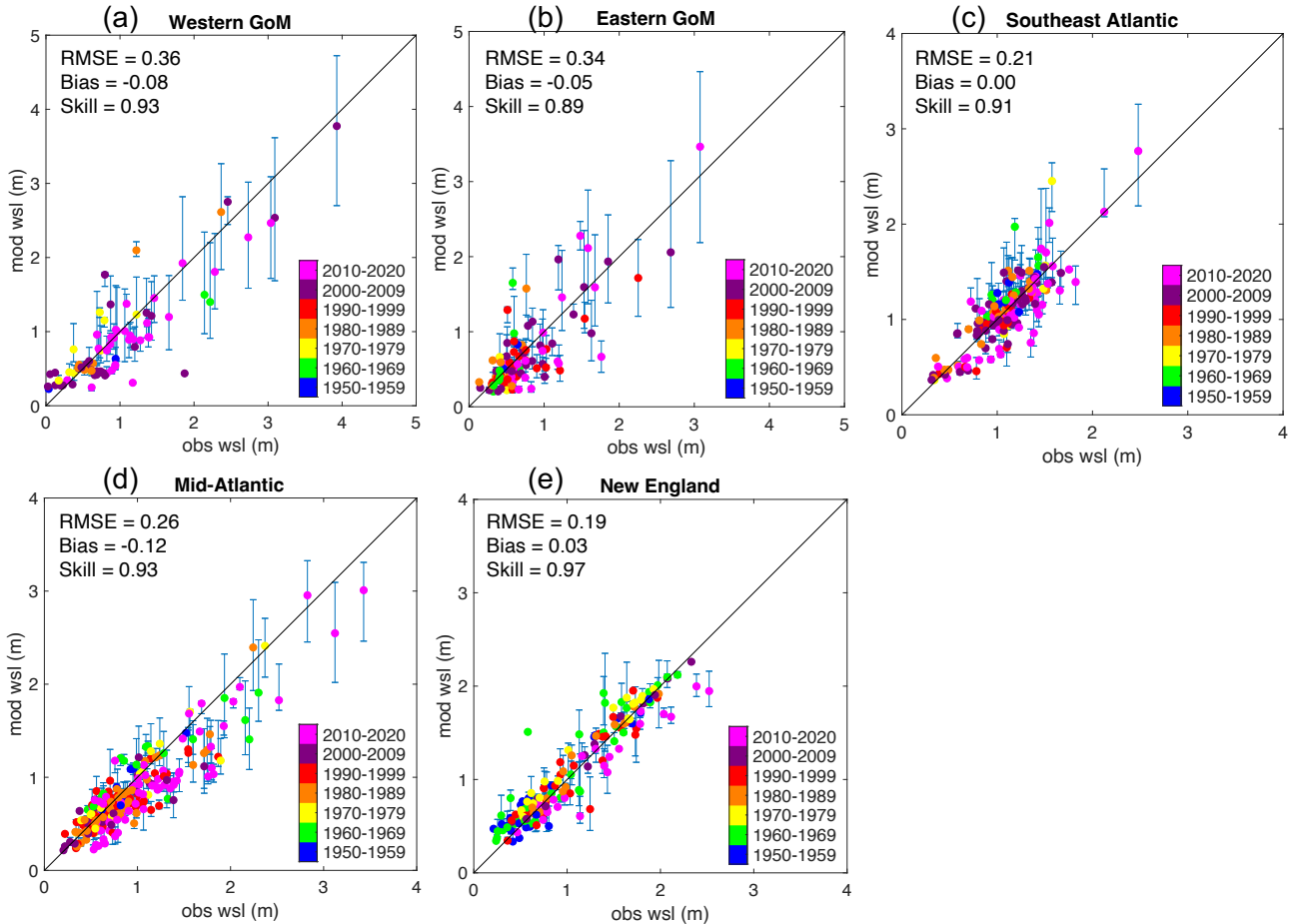
532 tide as shown in the next section (see Figure 6) Therefore, we use un-adjusted  
533 ERA5+CLE15  $R_{\max}$  estimates in conjunction with the low-high ranges developed in  
534 section 3.3.1.

535

### 536 *3.4 Modeled and observed storm tides*

537 In addition to developing a record of historical TC sizes, the second goal of our  
538 study is to develop a spatiotemporally continuous database of peak TC storm tides. We  
539 simulate peak storm tides using the ERA5+CLE15 size estimates and the ADCIRC  
540 hydrodynamic model (forced with the CLE15 wind model) and compare our modeled  
541 peak storm tides against peak water levels from 74 tidal gauges along the US coastline.  
542 Figure 6 shows scatterplots of observed and modeled peak storm tides, associated  
543 performance metrics, and error bars representing the low/high peak storm tides obtained  
544 from using the low/high  $R_{\max}$  estimates at each active tidal gauge within each coastline  
545 region, where the regions are defined in Figure 8. Each point is colored based on the  
546 decade in which the storm occurred. Across all regions of the coastline, the reconstructed  
547 storm tides match well against observed peak water levels, with skill scores ranging from  
548 0.89-0.97 and mean bias ranging from -0.12 – 0.03 m (where negative bias indicates  
549 model under prediction). Both the western and eastern Gulf of Mexico (GoM) have larger  
550 RMSE for peak storm tide estimates compared to locations along the Atlantic coast. The  
551 lower storm tide accuracy in the GoM is due to the coastline configuration and wide  
552 continental shelf, which causes storm tides to be highly sensitive to TC size in addition to  
553 TC intensity (Irish et al., 2008). Moreover, tidal amplitudes within the GoM are  
554 relatively small, so the wind-induced storm surge makes up a large component of the  
555 total water levels, while larger tidal ranges more strongly modulate total water levels  
556 along the Atlantic coast. Modeled storm tides along the GoM also tend to have larger  
557 uncertainty bars associated with a one standard deviation increase/decrease in  $R_{\max}$ ,  
558 which also demonstrates that storm tides here are sensitive to TC size. Along the  
559 southeast and middle Atlantic, there is smaller error in the peak storm tide estimates, as  
560 demonstrated by the smaller RMSE values. The modeled and simulated storm tides  
561 match very closely in the New England region because the tidal amplitudes are large in  
562 this region and consequently the wind-induced surge makes up a smaller component of

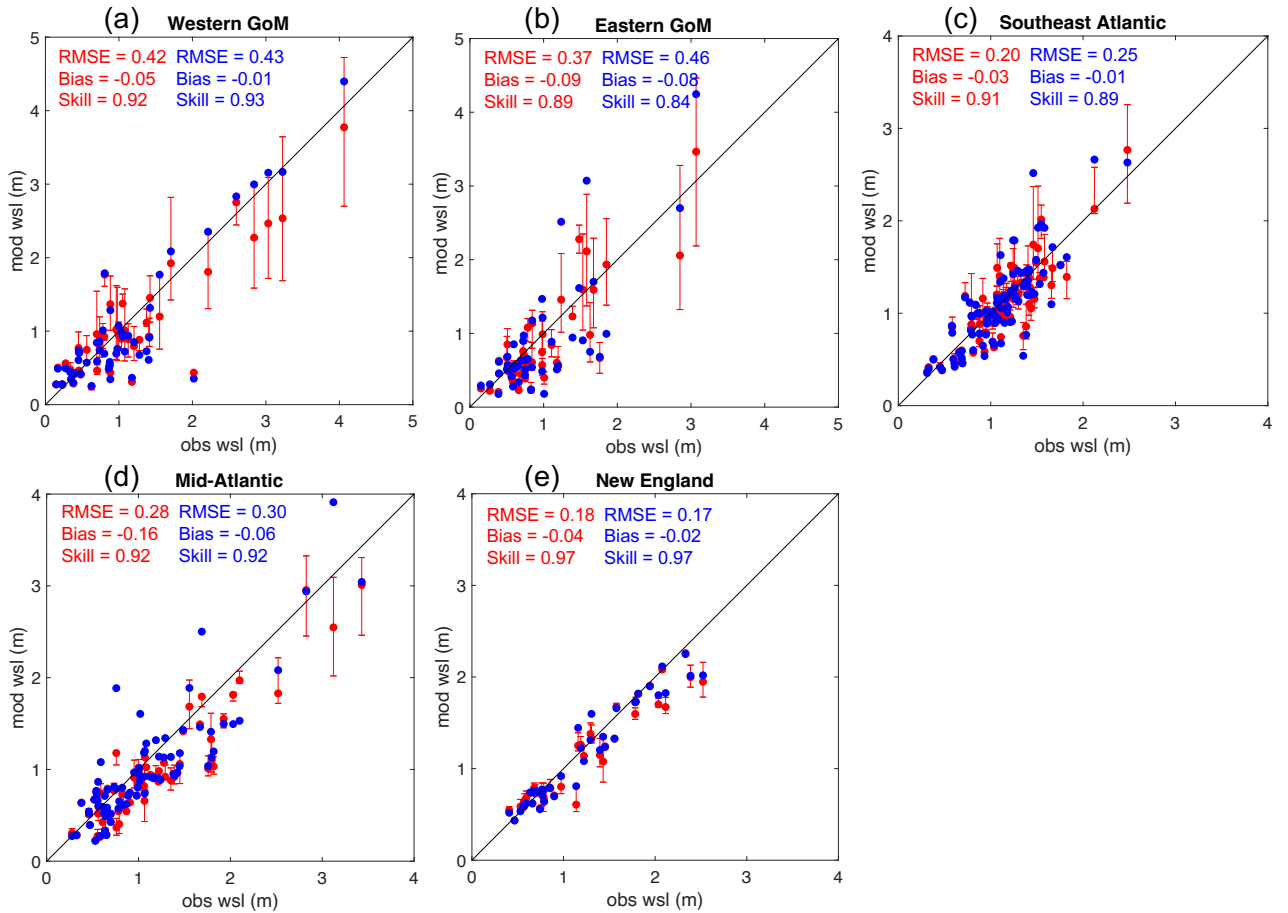
563 the total water levels. Despite these differences in performance across different coastal  
 564 regions, the comparisons shown in Figure 6 demonstrate that the models perform well for  
 565 both early storms (1950-1979; see performance in Figure S7) and more recent storms  
 566 (1980-2020).



567  
 568 **Figure 6:** Comparison of modeled peak storm tides and observed peak storm tides for all historical  
 569 TCs between 1950-2020 grouped into 5 regions: (a) Western Gulf of Mexico, (b) Eastern Gulf of  
 570 Mexico, (c) Southeast Atlantic, (d) Mid-Atlantic, and (e) New England. Points are colored by  
 571 decade and depict associated error bars (+/- one standard deviation of Rmax).  
 572

573 The errors between the observed and modeled storm tides could stem from  
 574 multiple sources including uncertainty in  $R_{max}$ , TC position, or intensity from IBTrACS  
 575 (Landsea and Franklin, 2013). Wave impacts, or errors stemming from the hydrodynamic  
 576 mesh and/or physics of the ADCIRC model may also contribute to storm tide errors.  
 577 Additionally, the parametric wind and pressure models used to represent the TC within  
 578 ADCIRC may not match perfectly against the true TC wind/pressure fields. Therefore, to  
 579 isolate the impact of the ERA5+CLE15  $R_{max}$  estimate procedure, Figure 7 shows similar

580 comparisons of modeled and observed peak storm tides from 2004-2020, where red dots  
581 are modeled using ERA5+CLE15 estimated sizes and blue dots are based on the  
582 IBTrACS size. The difference in performance between ERA5+CLE15 storm tides and  
583 IBTrACS storm tides is small across all regions of the coastline, and the Willmott skill is  
584 slightly higher when using the ERA5+CLE15  $R_{\max}$  values in the eastern GoM and  
585 southeast Atlantic. For all regions the ERA5+CLE15 storm tides have a larger negative  
586 bias compared to the IBTrACS storm tides, but the high storm tide events are equally  
587 well captured by ERA5+CLE15. The mean bias for the mid-Atlantic is -0.16 m when  
588 using ERA5+CLE15 to estimate  $R_{\max}$ , compared to -0.06 m when using the IBTrACS  
589  $R_{\max}$ . The slight underestimation of storm tides caused by using ERA5+CLE15 storm size  
590 estimates could be due to the CLE15 model's underestimation of  $R_{\max}$  at mid-high  
591 latitudes and for ET storms (discussed in Section 3.3). Nevertheless, Fig. 7 shows that  
592 using ERA5+CLE15 to estimate the storm size does not result in significantly worse  
593 storm tide predictions compared to using the IBTrACS data. The storm tide performance  
594 metrics obtained by using the ERA5+CLE15  $R_{\max}$  estimates are also similar to the  
595 performance metrics reported in Marsooli et al. (2018), which utilized the same basin-  
596 scale mesh as this study and modeled storm tides for TCs from 1988-2015 using  
597 Extended Best Track (Demuth et al., 2006)  $R_{\max}$ . Modeled peak storm tides from  
598 Marsooli et al. (2018) had an average RMSE, bias, and Willmott skill of 0.31, -0.04, and  
599 0.90, respectively. In comparison, we report an average RMSE, bias, and Willmott skill  
600 of 0.29, -0.07, and 0.92 for all TCs from 2004-2020.



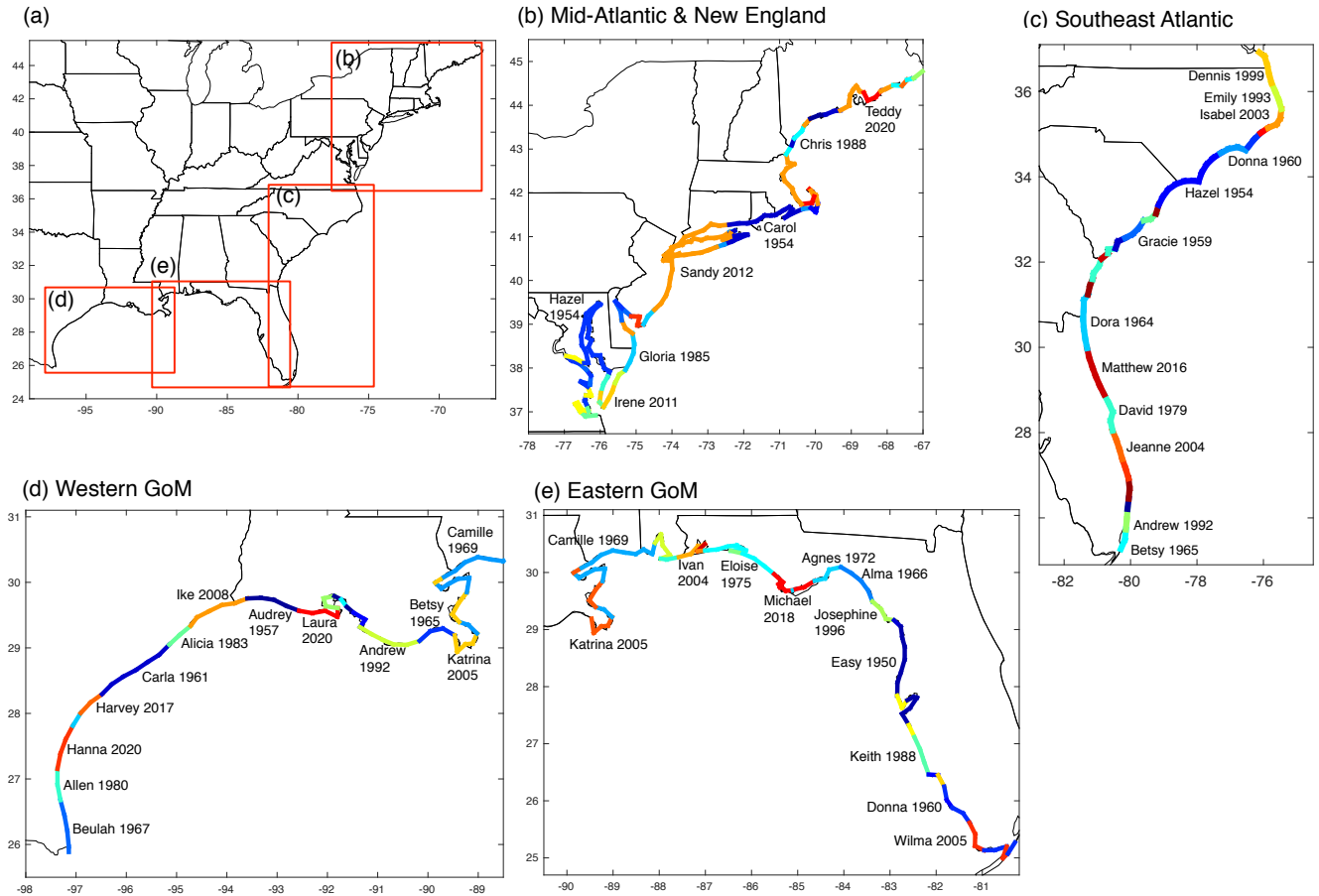
601

602 **Figure 7:** Comparison of modeled peak storm tides and observed peak storm tides for all historical  
 603 TCs between 2004-2020 grouped into 5 regions: (a) Western Gulf of Mexico, (b) Eastern Gulf of  
 604 Mexico, (c) Southeast Atlantic, (d) Mid-Atlantic, and (e) New England. Red points were  
 605 modeled using ERA5+CLE15 TC size and blue points were modeled used IBTrACS size data.  
 606

607 *3.5 Impact of TCs from 1950-1988 on storm surge hazard*

608 To demonstrate the potential value of our reconstructions, we investigate how  
 609 storm tides from TCs occurring between 1950-1987 can provide additional insight about  
 610 coastal storm surge hazard. We model storm tides from 467 landfalling TCs, 227 of  
 611 which occurred before 1988. Figure 8 shows which TCs caused the largest peak storm  
 612 tides along different regions of the coastline. Along the mid-Atlantic and New England,  
 613 Hurricane Sandy (2012) caused the highest storm tides for a large portion of the  
 614 coastline. However, Hurricanes Hazel (1954) and Carol (1954) caused the most extreme  
 615 storm surges in the Chesapeake Bay and Rhode Island, respectively. Hazel made landfall  
 616 near the South/North Carolina boarder as a category 4 storm, and caused the highest  
 617 storm tide levels along northern South Carolina and southern North Carolina, and in the

618 Chesapeake Bay. Hazel’s intense winds prior to landfall funneled large amounts of water  
 619 into the Chesapeake Bay and the resulting storm surge coincided with high tide, driving  
 620 water levels even higher.



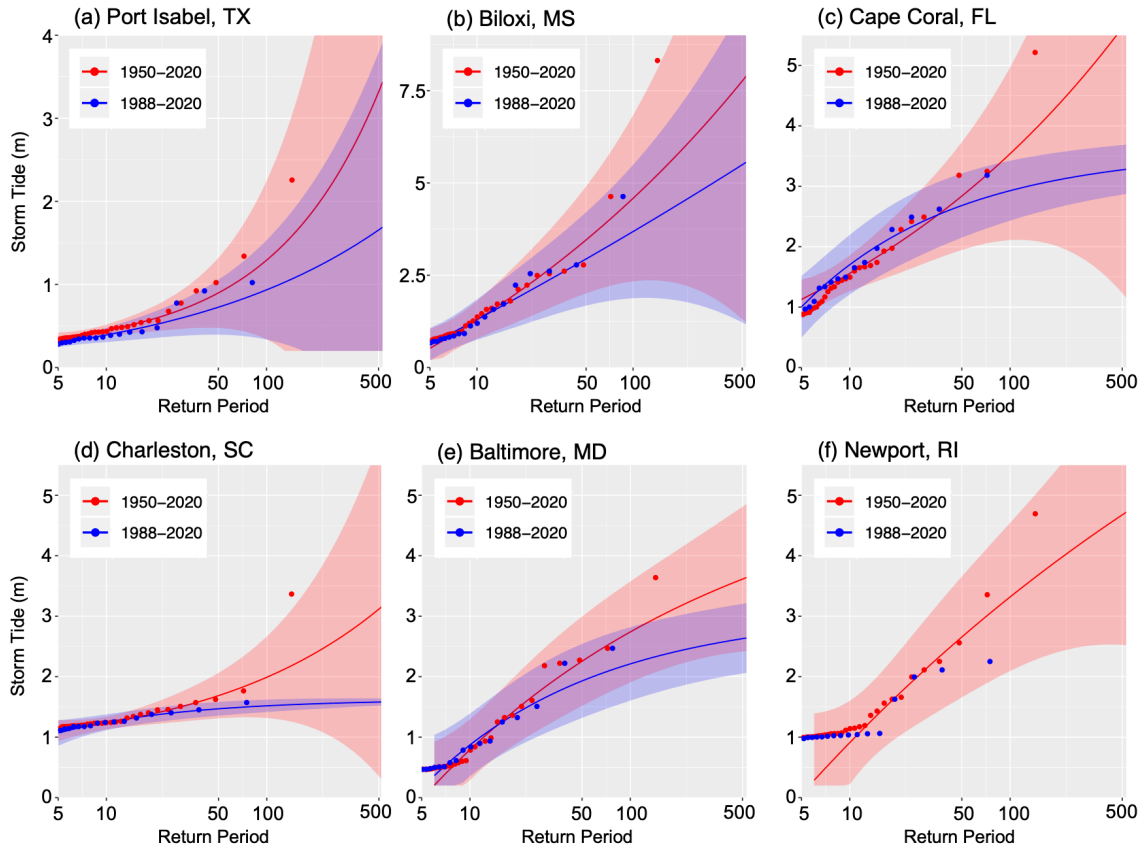
621  
 622 **Figure 8:** Storms that produced maximum modeled storm tides for different regions of the coastline  
 623 (a): (b) Mid-Atlantic and New England, (c) Southeast Atlantic, (d) Western Gulf of Mexico, (e)  
 624 Eastern Gulf of Mexico  
 625

626 In the southeast Atlantic (Fig. 8c) there are many storms before 1988 that caused  
 627 the highest storm tides along different portions of the coast, including Hazel (1954),  
 628 Gracie (1959), Dora (1964), and David (1979). Gracie made landfall nearly perpendicular  
 629 to the coast as a category 4 storm along the southern South Carolina coast, causing  
 630 widespread storm surge flooding despite arriving at low tide. In contrast, David moved  
 631 parallel to the east coast of Florida as a weak hurricane, but still induced large storm tides  
 632 in the Cape Canaveral region.

633 Similarly, along the eastern GoM (Fig. 8e) Camille (1969), Easy (1950) and  
 634 Donna (1960) caused extreme storm surges. Camille, which made landfall near the border

635 of Louisiana and Mississippi, was the second most intense storm to strike the US, and  
636 caused devastating storm tides that reached up to 6-9 m along the coastline of Mississippi  
637 (ESSA, 1969; NBS, 1971). Along the western GoM, Beulah (1967) and Carla (1961)  
638 were the most devastating pre-1988 TCs. Beulah was one of the most powerful  
639 hurricanes to hit the lower Texas coast, causing widespread storm surges and coastal  
640 erosion.

641 While Figure 8 illustrates which TCs caused the largest storm surge impacts, it  
642 does not tell us how the incorporation of TCs from 1950-1987 impacts our estimates of  
643 storm surge hazard. Incorporating a larger sample size of historical TCs occurring from  
644 1950 to present can enable better estimation of storm surge return periods at different  
645 coastal locations, especially at locations with a limited number of recent (post 1987) TC  
646 occurrences. Figure 9 compares storm tide return period curves at several coastal  
647 locations derived from modeled storm tides occurring from 1950-2020 (red) and similar  
648 curves derived from only 1988-2020 TCs (blue). The curves in Fig. 9 were calculated by  
649 fitting modeled storm tides with a generalized pareto distribution for the tail and  
650 assuming TC arrivals occur as a Poisson process (Lin et al., 2012; Lin et al., 2010;  
651 Marsooli et al., 2019). The shaded regions around each return period curve represent the  
652 95% confidence intervals calculated according to the Delta method (Coles, 2001). The  
653 locations in Figure 9 were chosen because there are significant differences between the  
654 return period curves derived from the entire dataset compared to the more recent subset  
655 of storms. At Port Isabel on the lower Texas coast, the extreme storm surges from Beulah  
656 (1967) as well as Allen (1980) cause the 100-year storm tide estimate to increase from  
657 0.97 m to 1.28 m above mean sea level. At Biloxi, MS, the extreme winds from Camille  
658 (1969) caused 8 m of storm tide, which is over 3 m higher than the second highest storm  
659 tide event (4.6 m caused by Katrina in 2005). The 100-year storm tide at Biloxi, MS  
660 based on all storms from 1950-2020 is 4.6 m, while the 100-year estimate for 1988-2020  
661 storms is only 3.7 m. Hurricane Camille is the primary data point causing an increase in  
662 100-year storm tide: the incorporation of Camille's storm tide alone increases the 100-  
663 year storm tide to 4.4 m.



664

665 **Figure 9:** Storm tide return levels at select coastal locations using TCs from 1950-2020 (red) and  
 666 using TCs from 1988-2020 (blue). Shading represents 95% confidence intervals and points  
 667 represent individual storms.  
 668

669         Incorporating a larger sample size of events can also impact the estimated shape  
 670 of the storm tide distribution at some locations. For example, at Cape Coral and  
 671 Charleston incorporating storm tides from 1950-1987 changes the estimated tail behavior  
 672 of the distribution from a bounded tail to an unbounded tail. Unbounded tail behavior  
 673 causes the storm tide return level to increase exponentially with increasing log return  
 674 period, albeit with higher uncertainty bounds as calculated through the Delta method. The  
 675 return period estimates for a bounded versus unbounded distribution diverge increasingly  
 676 for high storm tide values. For example, at Charleston the peak storm tide from Gracie  
 677 (1959) was around 3.3 m, which is estimated as a 600-year event using the 1950-2020  
 678 return level curve. However, if we use the 1988-2020 curve, Gracie's return period would  
 679 be undefined since the bounded tail distribution predicts zero probability for such a large  
 680 event to occur. At Newport, RI the top three storm tide events all occurred before 1987

681 with the largest storm tide caused by hurricane Carol (1954). Because TC occurrences  
682 from 1988-2020 at Newport are so limited, it is not possible to fit a GP distribution to the  
683 1988-2020 data. However, by incorporating the earlier TCs, it is possible to fit the GP  
684 distribution and obtain an estimate of the 100-year storm tide, which is 3.3 m.

685 The analysis presented here illustrates how the newly reconstructed storm tides  
686 from TCs occurring in 1950-1987 can provide valuable information about storm surge  
687 hazard across the US coastline. By developing continuous maps of peak storm tides,  
688 these reconstructions can supplement sparse gauge observations and provide a more  
689 complete understanding of historical TC storm surge hazard. Similarly, the reconstructed  
690 TC size data together with track and intensity data can be used to enhance estimates of  
691 historical TC wind (Wang et al., 2022) and rainfall, based on physical rainfall models  
692 (Feldmann et al., 2019; Xi et al., 2020; Zhu et al., 2013).

693

#### 694 **4 Discussion and Conclusions**

695 In this study we develop a database of reconstructed historical TC sizes and storm  
696 tides based on a combination of reanalysis data and physics-based modeling. Specifically,  
697 we demonstrate that the ERA5 reanalysis data can represent TC outer size with good  
698 accuracy compared to observations. We then show that the physics-based CLE15 model  
699 can reasonably reproduce the TC  $R_{max}$  using Best Track intensity information and  
700 reanalysis-based outer size. Finally, we utilize the size reconstructions to develop a  
701 dataset of modeled coastal storm tides for TCs making landfall between 1950-2020 and  
702 demonstrate that the modeled storm tides compare well against tidal gauge observations.

703 The TC reconstruction methodology demonstrated here can be used in a variety of  
704 future applications, including quantification of wind, surge, and rainfall hazard, as well  
705 multi-hazard assessment (Gori et al., 2022; Moftakhari et al., 2017; Nasr et al., 2021;  
706 Song et al., 2020; Wahl et al., 2015). The TC size data generated here for the North  
707 Atlantic can also be combined with track and intensity data, and high-resolution ocean  
708 and atmosphere models to conduct detailed hindcast analysis of extreme winds, rainfall  
709 and storm surges (Lin et al., 2010) for pre-1988 TCs impacting the US coastline. The  
710 reconstructed size and storm tide data could also be used as input data for TC impact  
711 models (Hatzikyriakou et al., 2016; Nofal et al., 2021; Pilkington and Mahmoud,

712 2016) to reconstruct economic losses from historical TCs and conduct TC risk analysis.  
713 The ERA5+CLE15 approach could also be applied to reconstruct sizes in other ocean  
714 basins where TC data may be more limited or discontinuous (Knaff et al., 2018; Kossin et  
715 al., 2013). The CLE15 model can be combined with climatological mean values of outer  
716 size (Chavas et al., 2016; Chavas and Emanuel, 2010) to reconstruct TC wind fields and  
717 storm surges for storms occurring before 1950, similar to the approach implemented in  
718 Lin et al. (2014). Finally, the approach described here could be utilized with output from  
719 general circulation models (GCMs) to evaluate changes in TC climatology and hazards  
720 resulting from different climate warming scenarios.

721 The TC size and storm tide reconstructions developed here may be impacted by  
722 limitations and uncertainties stemming from the ERA5 reanalysis data (discussed in  
723 sections 2.2 and 3.2), CLE15 wind model (section 3.3), and hydrodynamic model and  
724 mesh (section 3.4). Although there is higher uncertainty associated with the use of ERA5  
725 to represent 1950-1979 TCs, storm tide modeling results suggest that our approach can  
726 well-capture peak water levels induced by early TCs (Fig. S7). Similarly, despite some  
727 underestimation of  $R_{\max}$  for ET time steps (Fig. 3d), our modeling framework still  
728 accurately simulates peak storm tides along the Mid-Atlantic and New England coastlines  
729 (Fig 6d-e). Moreover, the ERA5+CLE15 approach performs with high skill and near-zero  
730 bias for TC time steps below 30N (Fig 3b) and on a storm-averaged basis (Fig. 3a),  
731 suggesting that our size reconstructions can reasonably represent pre-1988 TCs.

732

### 733 **Acknowledgements**

734 A.G. was supported by a National Defense Science & Engineering Graduate (NDSEG)  
735 fellowship from the US Department of Defense. N.L. was supported by National Science  
736 Foundation (NSF) grant number 1652448. D.C. was supported by NSF grant number  
737 AGS 1945113.

738

### 739 **Data Availability Statement**

740 All data utilized in this study come from publicly available repositories (cited in the  
741 manuscript). All data generated from this study, including estimated TC sizes and

742 modeled storm tides are deposited to the NSF DesignSafe-CI and can be freely assessed  
743 online ([DOI to be provided upon acceptance]).

744

745 **References**

746 Bass, B., Irza, J.N., Proft, J., Bedient, P., Dawson, C., 2017. Fidelity of the integrated  
747 kinetic energy factor as an indicator of storm surge impacts. *Natural Hazards*  
748 85, 575–595. <https://doi.org/10.1007/s11069-016-2587-3>

749 Berg, R., 2018. National Hurricane Center Tropical Cyclone Report. Hurricane Jose.  
750 Beven, J.L., Avila, L.A., Blake, E.S., Brown, D.P., Franklin, J.L., Knabb, R.D., Pasch, R.J.,  
751 Rhome, J.R., Stewart, S.R., 2008. Atlantic hurricane season of 2005. *Monthly*  
752 *Weather Review* 136, 1109–1173. <https://doi.org/10.1175/2007MWR2074.1>

753 Bian, G.F., Nie, G.Z., Qiu, X., 2021. How well is outer tropical cyclone size represented  
754 in the ERA5 reanalysis dataset? *Atmospheric Research* 249, 105339.  
755 <https://doi.org/10.1016/j.atmosres.2020.105339>

756 Blake, E., Kimberlain, T., Berg, R., Cangialosi, J., Beven II, J., 2013. Tropical Cyclone  
757 Report: Hurricane Sandy.

758 Blake, E.S., Zelinsky, D.A., 2017. Tropical Cyclone Report: Hurricane Harvey.

759 Chavas, D.R., Emanuel, K.A., 2010. A QuikSCAT climatology of tropical cyclone size.  
760 *Geophysical Research Letters* 37, 10–13.  
761 <https://doi.org/10.1029/2010GL044558>

762 Chavas, D.R., Knaff, J.A., 2022. A simple model for predicting the hurricane radius of  
763 maximum wind from outer size. *Weather and Forecasting* accepted, 1–20.

764 Chavas, D.R., Lin, N., 2016. A model for the complete radial structure of the tropical  
765 cyclone wind field. Part II: Wind field variability. *Journal of the Atmospheric*  
766 *Sciences* 73, 3093–3113. <https://doi.org/10.1175/JAS-D-15-0185.1>

767 Chavas, D.R., Lin, N., Dong, W., Lin, Y., 2016. Observed tropical cyclone size revisited.  
768 *Journal of Climate* 29, 2923–2939. <https://doi.org/10.1175/JCLI-D-15-0731.1>

769 Chavas, D.R., Lin, N., Emanuel, K., 2015. A model for the complete radial structure of  
770 the tropical cyclone wind field. Part I: Comparison with observed structure.  
771 *Journal of the Atmospheric Sciences* 72, 3647–3662.  
772 <https://doi.org/10.1175/JAS-D-15-0014.1>

773 Chavas, D.R., Reed, K.A., Knaff, J.A., 2017. Physical understanding of the tropical  
774 cyclone wind-pressure relationship. *Nature Communications* 8.  
775 <https://doi.org/10.1038/s41467-017-01546-9>

776 Chavas, D.R., Vigh, J., 2014. QSCAT-R: The QuikSCAT tropical cyclone radial structure  
777 dataset. NCAR Tech. Note TN-513+STR.

778 Chen, J., Chavas, D.R., 2020. The Transient Responses of an Axisymmetric Tropical  
779 Cyclone to Instantaneous Surface Roughening and Drying. *Journal of the*  
780 *Atmospheric Sciences* 77, 2807–2834. [https://doi.org/10.1175/JAS-D-19-](https://doi.org/10.1175/JAS-D-19-0320.1)  
781 0320.1

782 Cline, I., 1900. Special Report on the Galveston Hurricane of September 8, 1900.

783 Coles, S., 2001. *An Introduction to Statistical Modeling of Extreme Values*. Springer-  
784 Verlag, Bristol, UK.

785 Demuth, J.L., DeMaria, M., Knaff, J.A., 2006. Improvement of advanced microwave  
786 sounding unit tropical cyclone intensity and size estimation algorithms. *Journal*  
787 *of Applied Meteorology and Climatology* 45, 1573–1581.  
788 <https://doi.org/10.1175/JAM2429.1>

789 Done, J.M., Ge, M., J. Holland, G., Dima-West, I., Phibbs, S., R. Saville, G., Wang, Y., 2020.  
790 Modelling global tropical cyclone wind footprints. *Natural Hazards and Earth*  
791 *System Sciences* 20, 567–580. <https://doi.org/10.5194/nhess-20-567-2020>

792 Dullaart, J.C.M., Muis, S., Bloemendaal, N., Aerts, J.C.J.H., 2020. Advancing global  
793 storm surge modelling using the new ERA5 climate reanalysis. *Climate*  
794 *Dynamics* 54, 1007–1021. <https://doi.org/10.1007/s00382-019-05044-0>

795 Dullaart, J.C.M., Muis, S., Bloemendaal, N., Chertova, M. V., Couasnon, A., Aerts, J.C.J.H.,  
796 2021. Accounting for tropical cyclones more than doubles the global population  
797 exposed to low-probability coastal flooding. *Communications Earth &*  
798 *Environment* 2, 1–11. <https://doi.org/10.1038/s43247-021-00204-9>

799 ECMWF, 2021. ERA5 back extension 1950-1978 (Preliminary version): tropical  
800 cyclones are too intense [WWW Document]. URL  
801 [https://confluence.ecmwf.int/display/CKB/ERA5+back+extension+1950-](https://confluence.ecmwf.int/display/CKB/ERA5+back+extension+1950-1978+%28Preliminary+version%29%3A+tropical+cyclones+are+too+intense)  
802 [1978+%28Preliminary+version%29%3A+tropical+cyclones+are+too+intense](https://confluence.ecmwf.int/display/CKB/ERA5+back+extension+1950-1978+%28Preliminary+version%29%3A+tropical+cyclones+are+too+intense)  
803 (accessed 3.13.22).

804 Egbert, G.D., Erofeeva, S.Y., 2002. Efficient inverse modeling of barotropic ocean  
805 tides. *Journal of Atmospheric and Oceanic Technology* 19, 183–204.  
806 [https://doi.org/10.1175/1520-0426\(2002\)019<0183:EIMOBO>2.0.CO;2](https://doi.org/10.1175/1520-0426(2002)019<0183:EIMOBO>2.0.CO;2)

807 Emanuel, K., Rotunno, R., 2011. Self-stratification of tropical cyclone outflow. Part I:  
808 Implications for storm structure. *Journal of the Atmospheric Sciences* 68, 2236–  
809 2249. <https://doi.org/10.1175/JAS-D-10-05024.1>

810 ESSA, 1969. Hurricane Camille Preliminary Report.

811 Evans, C., Hart, R.E., 2008. Analysis of the wind field evolution associated with the  
812 extratropical transition of Bonnie (1998). *Monthly Weather Review* 136, 2047–  
813 2065. <https://doi.org/10.1175/2007MWR2051.1>

814 Evans, C., Wood, K.M., Aberson, S.D., Archambault, H.M., Milrad, S.M., Bosart, L.F.,  
815 Corbosiero, K.L., Davis, C.A., Pinto, J.R.D., Doyle, J., Fogarty, C., Galarneau, T.J.,  
816 Grams, C.M., Griffin, K.S., Gyakum, J., Hart, R.E., Kitabatake, N., Lentink, H.S.,  
817 McTaggart-Cowan, R., Perrie, W., Quinting, J.F.D., Reynolds, C.A., Riemer, M.,  
818 Ritchie, E.A., Sun, Y., Zhang, F., 2017. The extratropical transition of tropical  
819 cyclones. Part I: Cyclone evolution and direct impacts. *Monthly Weather Review*  
820 145, 4317–4344. <https://doi.org/10.1175/MWR-D-17-0027.1>

821 Feldmann, M., Emanuel, K., Zhu, L., Lohmann, U., 2019. Estimation of atlantic tropical  
822 cyclone rainfall frequency in the United States. *Journal of Applied Meteorology*  
823 *and Climatology* 58, 1853–1866. <https://doi.org/10.1175/JAMC-D-19-0011.1>

824 Fritz, H.M., Blount, C., Sokoloski, R., Singleton, J., Fuggle, A., McAdoo, B.G., Moore, A.,  
825 Grass, C., Tate, B., 2007. Hurricane Katrina storm surge distribution and field  
826 observations on the Mississippi Barrier Islands. *Estuarine, Coastal and Shelf*  
827 *Science* 74, 12–20. <https://doi.org/10.1016/j.ecss.2007.03.015>

828 Gori, A., Lin, N., Xi, D., Emanuel, K., 2022. Tropical cyclone climatology change greatly  
829 exacerbates US extreme rainfall–surge hazard. *Nature Climate Change* 12, 171–  
830 178. <https://doi.org/10.1038/s41558-021-01272-7>

831 Haigh, I.D., MacPherson, L.R., Mason, M.S., Wijeratne, E.M.S., Pattiaratchi, C.B.,  
832 Crompton, R.P., George, S., 2014. Estimating present day extreme water level  
833 exceedance probabilities around the coastline of Australia: Tropical cyclone-

834 induced storm surges. *Climate Dynamics* 42, 139–157.  
835 <https://doi.org/10.1007/s00382-012-1653-0>

836 Halverson, J.B., Rabenhorst, T., 2013. Hurricane Sandy: The Science and Impacts of a  
837 Superstorm. *Weatherwise* 66, 14–23.  
838 <https://doi.org/10.1080/00431672.2013.762838>

839 Hart, R.E., Evans, J.L., 2001. A climatology of the extratropical transition of Atlantic  
840 tropical cyclones. *Journal of Climate* 14, 546–564.  
841 [https://doi.org/10.1175/1520-0442\(2001\)014<0546:ACOTET>2.0.CO;2](https://doi.org/10.1175/1520-0442(2001)014<0546:ACOTET>2.0.CO;2)

842 Hatzikyriakou, A., Lin, N., Gong, J., Xian, S., Hu, X., Kennedy, A., 2016. Component-  
843 Based Vulnerability Analysis for Residential Structures Subjected to Storm  
844 Surge Impact from Hurricane Sandy. *Natural Hazards Review* 17, 05015005.  
845 [https://doi.org/10.1061/\(asce\)nh.1527-6996.0000205](https://doi.org/10.1061/(asce)nh.1527-6996.0000205)

846 Hersbach, H., Bell, B., Berrisford, P., Hirahara, S., Horányi, A., Muñoz-Sabater, J.,  
847 Nicolas, J., Peubey, C., Radu, R., Schepers, D., Simmons, A., Soci, C., Abdalla, S.,  
848 Abellan, X., Balsamo, G., Bechtold, P., Biavati, G., Bidlot, J., Bonavita, M., De  
849 Chiara, G., Dahlgren, P., Dee, D., Diamantakis, M., Dragani, R., Flemming, J.,  
850 Forbes, R., Fuentes, M., Geer, A., Haimberger, L., Healy, S., Hogan, R.J., Hólm, E.,  
851 Janisková, M., Keeley, S., Laloyaux, P., Lopez, P., Lupu, C., Radnoti, G., de Rosnay,  
852 P., Rozum, I., Vamborg, F., Villaume, S., Thépaut, J.N., 2020. The ERA5 global  
853 reanalysis. *Quarterly Journal of the Royal Meteorological Society* 146, 1999–  
854 2049. <https://doi.org/10.1002/qj.3803>

855 Hlywiak, J., Nolan, D.S., 2021. The Response of the Near-Surface Tropical Cyclone  
856 Wind Field to Inland Surface Roughness Length and Soil Moisture Content  
857 during and after Landfall. *Journal of the Atmospheric Sciences* 78, 983–1000.  
858 <https://doi.org/10.1175/JAS-D-20-0211.1>

859 Hodges, K., Cobb, A., Vidale, P.L., 2017. How well are tropical cyclones represented in  
860 reanalysis datasets? *Journal of Climate* 30, 5243–5264.  
861 <https://doi.org/10.1175/JCLI-D-16-0557.1>

862 Holland, G., 1980. An analytical model of wind and pressure profiles in hurricanes.  
863 *Monthly Weather Review* 108, 1212–1218.

864 Huffman, G.J., Pendergrass, A., NCAR, 2021. The Climate Data Guide: TRMM: Tropical  
865 Rainfall Measuring Mission [WWW Document].  
866 Irish, J.L., Resio, D.T., Ratcliff, J.J., 2008. The influence of storm size on hurricane  
867 surge. *Journal of Physical Oceanography* 38, 2003–2013.  
868 <https://doi.org/10.1175/2008JPO3727.1>  
869 Jones, S.C., Harr, P.A., Abraham, J., Bosart, L.F., Bowyer, P.J., Evans, J.L., Hanley, D.E.,  
870 Hanstrum, B.N., Hart, R.E., Lalaurette, F., Sinclair, M.R., Smith, R.K., Thorncroft,  
871 C., 2003. The extratropical transition of tropical cyclones: Forecast challenges,  
872 current understanding, and future directions. *Weather and Forecasting* 18,  
873 1052–1092. [https://doi.org/10.1175/1520-](https://doi.org/10.1175/1520-0434(2003)018<1052:TETOTC>2.0.CO;2)  
874 [0434\(2003\)018<1052:TETOTC>2.0.CO;2](https://doi.org/10.1175/1520-0434(2003)018<1052:TETOTC>2.0.CO;2)  
875 Knabb, R.D., Rhome, J.R., Brown, D.P., 2005. Tropical Cyclone Report: Hurricane  
876 Katrina.  
877 Knaff, J.A., Sampson, C.R., Musgrave, K.D., 2018. Statistical tropical cyclone wind radii  
878 prediction using climatology and persistence: Updates for the western North  
879 Pacific. *Weather and Forecasting* 33, 1093–1098.  
880 <https://doi.org/10.1175/WAF-D-18-0027.1>  
881 Knaff, J.A., Zehr, R.M., 2007. Reexamination of tropical cyclone wind-pressure  
882 relationships. *Weather and Forecasting* 22, 71–88.  
883 <https://doi.org/10.1175/WAF965.1>  
884 Knapp, K.R., Kruk, M.C., Levinson, D.H., Diamond, H.J., Neumann, C.J., 2010. The  
885 international best track archive for climate stewardship (IBTrACS). *Bull Am*  
886 *Meteorol Soc* 91, 363–376. <https://doi.org/10.1175/2009BAMS2755.1>  
887 Kossin, J.P., Olander, T.L., Knapp, K.R., 2013. Trend analysis with a new global record  
888 of tropical cyclone intensity. *Journal of Climate* 26, 9960–9976.  
889 <https://doi.org/10.1175/JCLI-D-13-00262.1>  
890 Landsea, C.W., Anderson, C., Charles, N., Clark, G., Dunion, J., Fernandez-Partagas, J.,  
891 Hungerford, P., Neumann, C., Zimmer, M., 2004. The Atlantic hurricane database  
892 re-analysis project: Documentation for the 1851-1910 alterations and additions  
893 to the HURDAT database. *Hurricanes and Typhoons: Past, Present, and Future*  
894 177–221.

895 Landsea, C.W., Franklin, J.L., 2013. Atlantic hurricane database uncertainty and  
896 presentation of a new database format. *Monthly Weather Review* 141, 3576–  
897 3592. <https://doi.org/10.1175/MWR-D-12-00254.1>

898 Lin, N., Chavas, D., 2012. On hurricane parametric wind and applications in storm  
899 surge modeling. *Journal of Geophysical Research Atmospheres* 117, 1–19.  
900 <https://doi.org/10.1029/2011JD017126>

901 Lin, N., Emanuel, K., Oppenheimer, M., Vanmarcke, E., 2012. Physically based  
902 assessment of hurricane surge threat under climate change. *Nature Climate*  
903 *Change* 2, 462–467. <https://doi.org/10.1038/nclimate1389>

904 Lin, N., Emanuel, K.A., Smith, J.A., Vanmarcke, E., 2010. Risk assessment of hurricane  
905 storm surge for New York City. *Journal of Geophysical Research Atmospheres*  
906 115, 1–11. <https://doi.org/10.1029/2009JD013630>

907 Lin, N., Lane, P., Emanuel, K.A., Sullivan, R.M., Donnelly, J.P., 2014. Heightened  
908 hurricane surge risk in northwest Florida revealed from climatological-  
909 hydrodynamic modeling and paleorecord reconstruction. *Journal of*  
910 *Geophysical Research* 119, 8606–8623.  
911 <https://doi.org/10.1002/2014JD021584>

912 Lin, Ning, Smith, J.A., Villarini, G., Marchok, T.P., Baeck, M.L., 2010. Modeling Extreme  
913 Rainfall, Winds, and Surge from Hurricane Isabel (2003). *Weather and*  
914 *Forecasting* 25, 1342–1361. <https://doi.org/10.1175/2010waf2222349.1>

915 Lin, Y., Mitchell, K.E., 2005. The NCEP Stage II/IV hourly precipitation analyses:  
916 Development and applications, in: 19th Conf. on Hydrology. Amer. Meteor. Soc.,  
917 San Diego, CA.

918 Liu, M., Vecchi, G.A., Smith, J.A., Knutson, T.R., 2019. Causes of large projected  
919 increases in hurricane precipitation rates with global warming. *npj Climate and*  
920 *Atmospheric Science* 2, 1–5. <https://doi.org/10.1038/s41612-019-0095-3>

921 Luettich, R.A., Westerink, J.J., Scheffner, N.W., 1992. ADCIRC: An advanced three-  
922 dimensional circulation model for shelves, coasts, and estuaries. Report 1:  
923 Theory and methodology of ADCIRC-2DDI and ADCIRC-3DL. Vicksburg, Miss.

924 Marsooli, R., Lin, N., 2018. Numerical Modeling of Historical Storm Tides and Waves  
925 and Their Interactions Along the U.S. East and Gulf Coasts. *Journal of*

926 Geophysical Research: Oceans 3844–3874.  
927 <https://doi.org/10.1029/2017JC013434>

928 Marsooli, R., Lin, N., Emanuel, K., Feng, K., 2019. Climate change exacerbates  
929 hurricane flood hazards along US Atlantic and Gulf Coasts in spatially varying  
930 patterns. *Nature Communications* 10, 1–9. [https://doi.org/10.1038/s41467-](https://doi.org/10.1038/s41467-019-11755-z)  
931 [019-11755-z](https://doi.org/10.1038/s41467-019-11755-z)

932 Menne, M.J., Durre, I., Vose, R.S., Gleason, B.E., Houston, T.G., 2012. An overview of  
933 the global historical climatology network-daily database. *Journal of*  
934 *Atmospheric and Oceanic Technology* 29, 897–910.  
935 <https://doi.org/10.1175/JTECH-D-11-00103.1>

936 Merrill, R., 1984. A Comparison of Large and Small Tropical Cyclones. *Monthly*  
937 *Weather Review* 112, 1408–1418.

938 Moftakhari, H.R., Salvadori, G., AghaKouchak, A., Sanders, B.F., Matthew, R.A., 2017.  
939 Compounding effects of sea level rise and fluvial flooding. *Proceedings of the*  
940 *National Academy of Sciences* 114, 9785–9790.  
941 <https://doi.org/10.1073/pnas.1620325114>

942 Muis, S., Lin, N., Verlaan, M., Winsemius, H.C., Ward, P.J., Aerts, J.C.J.H., 2019.  
943 Spatiotemporal patterns of extreme sea levels along the western North-Atlantic  
944 coasts. *Scientific Reports* 9, 1–12. [https://doi.org/10.1038/s41598-019-40157-](https://doi.org/10.1038/s41598-019-40157-w)  
945 [w](https://doi.org/10.1038/s41598-019-40157-w)

946 Nasr, A.A., Wahl, T., Rashid, M.M., Camus, P., Haigh, I.D., 2021. Assessing the  
947 dependence structure between oceanographic, fluvial, and pluvial flooding  
948 drivers along the United States coastline. *Hydrology and Earth System Sciences*  
949 25, 6203–6222. <https://doi.org/10.5194/hess-25-6203-2021>

950 NBS, 1971. NBS Technical Note 569: Hurricane Camille - August 1969. Washington,  
951 D. C.

952 Needham, H.F., Keim, B.D., 2012. A storm surge database for the US Gulf Coast.  
953 *International Journal of Climatology* 32, 2108–2123.  
954 <https://doi.org/10.1002/joc.2425>

955 Needham, H.F., Keim, B.D., Sathiaraj, D., 2015. A review of tropical cyclone-generated  
956 storm surges: Global data sources, observations, and impacts. *Reviews of*  
957 *Geophysics* 53, 545–591. <https://doi.org/10.1002/2014RG000477>

958 Nguyen, L.T., Molinari, J., Thomas, D., 2014. Evaluation of tropical cyclone center  
959 identification methods in numerical models. *Monthly Weather Review* 142,  
960 4326–4339. <https://doi.org/10.1175/MWR-D-14-00044.1>

961 Nofal, O.M., van de Lindt, J.W., Do, T.Q., Yan, G., Hamideh, S., Cox, D.T., Dietrich, J.C.,  
962 2021. Methodology for Regional Multihazard Hurricane Damage and Risk  
963 Assessment. *Journal of Structural Engineering* 147, 04021185.  
964 [https://doi.org/10.1061/\(asce\)st.1943-541x.0003144](https://doi.org/10.1061/(asce)st.1943-541x.0003144)

965 Pilkington, S.F., Mahmoud, H.N., 2016. Using artificial neural networks to forecast  
966 economic impact of multi-hazard hurricane-based events. *Sustainable and*  
967 *Resilient Infrastructure* 1, 63–83.  
968 <https://doi.org/10.1080/23789689.2016.1179529>

969 Powell, M.D., Houston, S.H., Amat, L.R., Morisseau-Leroy, N., 1998. The HRD real-time  
970 hurricane wind analysis system. *Journal of Wind Engineering and Industrial*  
971 *Aerodynamics* 77–78, 53–64. [https://doi.org/10.1016/S0167-6105\(98\)00131-](https://doi.org/10.1016/S0167-6105(98)00131-7)  
972 7

973 Pugh, D., 1987. *Tides, Surges and Mean Sea-Level*. John Wiley & Sons, Chichester.

974 Ramos-Valle, A.N., Curchitser, E.N., Bruyère, C.L., 2020. Impact of Tropical Cyclone  
975 Landfall Angle on Storm Surge Along the Mid-Atlantic Bight. *Journal of*  
976 *Geophysical Research: Atmospheres* 125, 1–19.  
977 <https://doi.org/10.1029/2019JD031796>

978 Schenkel, B.A., Hart, R.E., 2012. An examination of tropical cyclone position,  
979 intensity, and intensity life cycle within atmospheric reanalysis datasets.  
980 *Journal of Climate* 25, 3453–3475. <https://doi.org/10.1175/2011JCLI4208.1>

981 Schenkel, B.A., Lin, N., Chavas, D., Oppenheimer, M., Brammer, A., 2017. Evaluating  
982 outer tropical cyclone size in reanalysis datasets using QuikSCAT data. *Journal*  
983 *of Climate* 30, 8745–8762. <https://doi.org/10.1175/JCLI-D-17-0122.1>

984 Schenkel, B.A., Lin, N., Chavas, D., Vecchi, G.A., Oppenheimer, M., Brammer, A., 2018.  
985 Lifetime evolution of outer tropical cyclone size and structure as diagnosed

986 from reanalysis and climate model data. *Journal of Climate* 31, 7985–8004.  
987 <https://doi.org/10.1175/JCLI-D-17-0630.1>

988 Smith, A.B., Katz, R.W., 2013. US billion-dollar weather and climate disasters: Data  
989 sources, trends, accuracy and biases. *Natural Hazards* 67, 387–410.  
990 <https://doi.org/10.1007/s11069-013-0566-5>

991 Song, J.Y., Alipour, A., Moftakhari, H.R., Moradkhani, H., 2020. Toward a more  
992 effective hurricane hazard communication. *Environmental Research Letters* 15.  
993 <https://doi.org/10.1088/1748-9326/ab875f>

994 Stiles, B.W., Danielson, R.E., Poulsen, W.L., Brennan, M.J., Hristova-Veleva, S., Shen,  
995 T.P., Fore, A.G., 2014. Optimized tropical cyclone winds from quikscat: A neural  
996 network approach. *IEEE Transactions on Geoscience and Remote Sensing* 52,  
997 7418–7434. <https://doi.org/10.1109/TGRS.2014.2312333>

998 Taylor, K.E., 2001. Summarizing multiple aspects of model performance in a single  
999 diagram. *Journal of Geophysical Research* 106, 7183–7192.

1000 Thomas, A., Dietrich, J.C., Asher, T.G., Bell, M., Blanton, B.O., Copeland, J.H., Cox, A.T.,  
1001 Dawson, C.N., Fleming, J.G., Luettich, R.A., 2019. Influence of storm timing and  
1002 forward speed on tides and storm surge during Hurricane Matthew. *Ocean*  
1003 *Modelling* 137, 1–19. <https://doi.org/10.1016/j.ocemod.2019.03.004>

1004 Wahl, T., Jain, S., Bender, J., Meyers, S.D., Luther, M.E., 2015. Increasing risk of  
1005 compound flooding from storm surge and rainfall for major US cities. *Nature*  
1006 *Climate Change* 1–6. <https://doi.org/10.1038/NCLIMATE2736>

1007 Westerink, J.J., Luettich, R.A., Blain, C.A., Scheffner, N.W., 1992. ADCIRC: An advanced  
1008 three-dimensional circulation model for shelves, coasts, and estuaries. Report  
1009 2: User’s Manual for ADCIRC-2DDI. Vicks- burg, Miss.

1010 Willmott, C.J., 1981. On the validation of models. *Physical Geography* 2, 184–194.  
1011 <https://doi.org/10.1080/02723646.1981.10642213>

1012 Willoughby, H.E., Darling, R.W.R., Rahn, M.E., 2006. Parametric representation of the  
1013 primary hurricane vortex. Part II: A new family of sectionally continuous  
1014 profiles. *Monthly Weather Review* 134, 1102–1120.  
1015 <https://doi.org/10.1175/MWR3106.1>

1016 Woodruff, J.D., Irish, J.L., Camargo, S.J., 2013. Coastal flooding by tropical cyclones  
1017 and sea-level rise. *Nature* 504, 44–52. <https://doi.org/10.1038/nature12855>

1018 Xi, D., Lin, N., Smith, J., 2020. Evaluation of a physics-based tropical cyclone rainfall  
1019 model for risk assessment. *Journal of Hydrometeorology* 21, 2197–2218.  
1020 <https://doi.org/10.1175/JHM-D-20-0035.1>

1021 Zhang, W., Villarini, G., Vecchi, G.A., Smith, J.A., 2018. Urbanization exacerbated the  
1022 rainfall and flooding caused by hurricane Harvey in Houston. *Nature* 563, 384–  
1023 388. <https://doi.org/10.1038/s41586-018-0676-z>

1024 Zhu, L., Quiring, S.M., Emanuel, K.A., 2013. Estimating tropical cyclone precipitation  
1025 risk in Texas. *Geophysical Research Letters* 40, 6225–6230.  
1026 <https://doi.org/10.1002/2013GL058284>

1027